Daily monitoring of Effective Green Area Index and Vegetation Chlorophyll Content from continuous acquisitions of a multi-band spectrometer over winter wheat

Wenjuan Li, Marie Weiss, Sylvain Jay, Shanshan Wei, Na Zhao, Alexis Comar, Raul Lopez Lozano, Benoit de Solan, Qiangyi Yu, Wenbin Wu, et al.

▶ **To cite this version:**

Wenjuan Li, Marie Weiss, Sylvain Jay, Shanshan Wei, Na Zhao, et al.. Daily monitoring of Effective Green Area Index and Vegetation Chlorophyll Content from continuous acquisitions of a multi-band spectrometer over winter wheat. Remote Sensing of Environment, 2024, 300 (113883), pp.1-47. 10.1016/j.rse.2023.113883 . hal-04315243

HAL Id: hal-04315243
https://hal.inrae.fr/hal-04315243

Submitted on 30 Nov 2023

HAL is a multi-disciplinary open access archive for the deposit and dissemination of scientific research documents, whether they are published or not. The documents may come from teaching and research institutions in France or abroad, or from public or private research centers.

L'archive ouverte pluridisciplinaire **HAL**, est destinée au dépôt et à la diffusion de documents scientifiques de niveau recherche, publiés ou non, émanant des établissements d'enseignement et de recherche français ou étrangers, des laboratoires publics ou privés.

Distributed under a Creative Commons Attribution - NonCommercial - NoDerivatives 4.0 International License

Daily monitoring of Effective Green Area Index and Vegetation Chlorophyll Content from continuous acquisitions of a multi-band spectrometer over winter wheat

Wenjuan Li [a*], Marie Weiss [b], Sylvain Jay [b], Shanshan Wei [c], Na Zhao [d], Alexis Comar [e], Raul Lopez-Lozano [b], Benoit De Solan [f], Qiangyi Yu [a], Wenbin Wu [a*] and Frédéric Baret [b]

[a] *State Key Laboratory of Efficient Utilization of Arid and Semi-arid Arable Land in Northern China, the Institute of Agricultural Resources and Regional Planning, Chinese Academy of Agricultural Sciences, Beijing 100081, China*

[b] *UMR EMMAH 1114, INRAE, Avignon Université, F-84000, Avignon, France*

[c] *Centre for Remote Imaging, Sensing and Processing, National University of Singapore, Singapore 119076, Singapore*

[d] *State Key Laboratory of Resources and Environmental Information System, Institute of Geographic Sciences and Natural Resources Research, Chinese Academy of Sciences, Beijing 100101, China*

[e] *HIPHEN SAS, 120 Rue Jean Dausset, Site Agroparc, 84140 Avignon, France*

[f] *Arvalis, Institut du végétal, 228, route de l'aérodrome - CS 40509, 84914 Avignon Cedex 9, France*

Corresponding authors:

Wenjuan Li

Email address: liwenjuan01@caas.cn

Wenbin Wu

Email address: wuwenbin@caas.cn

State Key Laboratory of Efficient Utilization of Arid and Semi-arid Arable Land in Northern China, the Institute of Agricultural Resources and Regional Planning, Chinese Academy of Agricultural Sciences, Beijing 100081, China

Abstract

Green area index (GAI), leaf chlorophyll content (LCC) and canopy chlorophyll content (CCC) are key variables that are closely related to crop growth. Concurrent and continuous monitoring of GAI, LCC and CCC is critical to keep consistency among variables and make decisions for field precision managements. Previous studies have developed several instruments and algorithms to monitor continuous GAI, while the autonomous monitoring of three variables simultaneously has been lacking. This study presents a novel algorithm to retrieve daily GAI, LCC and CCC from continuous directional observations acquired by a fixed and economic affordable multi-band spectrometer (6 bands covering red, red-edge and near infrared domains) and a photosynthetically active radiation (PAR) sensor in the field. It is composed of three main steps, corresponding to three crucial questions when retrieving variables under natural environments using multi-band spectrometer installed on a near-surface platform: diffuse fraction in each spectral band, radiometric calibration and diurnal sun variation of daily acquisitions. First, we estimated diffuse fraction in each spectral band from the relationship with PAR diffuse fraction based on simulations of the 6S atmospheric radiative transfer model. Second, we computed the relative value of each band to the reference of mean of measurements on all six bands from near-surface measurements, in place of absolute radiometric calibration to limit the influence of changing illumination conditions. In the third step, we combined PROSAIL canopy radiative transfer model and kernel-driven models to retrieved GAI, LCC and CCC from artificial neural network using above spectral diffuse fraction and diurnal multi-angle relative observations. The algorithm was evaluated over 43 IoTA (Internet of things for Agriculture) systems that were installed in 29 wheat fields in France from March to May 2019. Results showed that our method provides good estimates of GAI with root mean square error (RMSE) of 0.54, relative RMSE (RRMSE) of 26.95%, R^2 of 0.86, LCC (RMSE = 12.06 µg/cm^2, RRMSE = 33.34%, R^2 = 0.52) and CCC (RMSE = 0.23 g/m^2, RRMSE = 24.58%, R^2 = 0.93). This study shows great potentials for concurrent estimates of GAI, LCC and CCC from continuous ground measurements. It will be useful over other vegetations or other near-surface platforms for simultaneous estimations of biophysical variables.

Keywords:

Green Area Index (GAI), Leaf Chlorophyll Content (LCC), Canopy Chlorophyll Content (CCC), Daily measurements, Wheat, Near-surface system

1 Introduction

The world population is expected to reach about 10 billion by the end of 2050 (FAO, 2017). This will require a huge boost of agricultural production to satisfy the population needs. To secure food supplies for the future and keep the sustainability of natural resources involved, agricultural technologies are rapidly evolving towards to a new paradigm-Agriculture 4.0 (Santos Valle and Kienzle, 2020). Daily, continuous and autonomous monitoring of crop state using near-surface monitoring system is a key component of this paradigm (Raj et al., 2021). Farmers could benefit from the daily measurements to monitor fields remotely, especially for those with inconvenient access. Sudden changes due to pests or diseases within the field of view of Internet-of-Things (IoT) systems can be promptly detected and intervened (Ojha et al., 2015). In addition, daily variables estimated from measurements can feed decision tools for precision fertilization, irrigation and harvest managements (Lemaire et al., 2021).

Leaf area index (LAI), leaf chlorophyll content (LCC) and canopy chlorophyll content (CCC) are three important variables that are closely related to the crop status. LAI represents one half of the total green leaf area per unit horizontal ground surface area (Chen and Black, 1992) and it is an essential vegetation structural variable in several functioning processes (GCOS, 2011). In this study, we focus on Green Area Index (GAI) in place of LAI since we consider all the green parts of the plants that are involved in photosynthesis, including green leaves, stems and reproductive organs (Baret et al., 2010). LCC is the amount of chlorophyll *a* and *b* per unit leaf area (μg/cm^2 leaf) and CCC is the canopy integrated chlorophyll content, which can be approximated as multiplication of GAI and LCC. Both are important physiological indicators and provide indirect estimations of leaf/canopy nitrogen content (Berger et al., 2020; Croft et al., 2017; Gitelson et al., 2014; Verrelst et al., 2021). In the context of precision agriculture, continuous and concurrent in-situ observations of GAI and LCC are key to achieve consistent estimates of CCC and capture crop structure and physiological status simultaneously (Darvishzadeh et al., 2012; M. Weiss et al., 2020; P. Zhang et al., 2021).

Substantial efforts have been made to develop automatic ground monitoring systems for observations of these variables. Continuous ground GAI can be measured through transmittance in a single band, e.g., PASTIS-57 (Fang et al., 2018; Raymaekers et al., 2014) and 4S (Kim et al., 2019), through above and below canopy photosynthetically active radiation (PAR)(Rogers et al., 2021), through gap fraction in RGB images (Chen et al., 2022; Wang et al., 2022), or digital camera traps (Chianucci et al., 2021; Niu et al., 2021; Ryu et al.,

2012). However, all these systems focus on GAI estimations solely and do not allow to provide concurrent continuous estimations of LCC and CCC. As LCC has been demonstrated to be strongly related to reflectance in red-edge and NIR bands (Gitelson, 2005; Main et al., 2011), using transmittance from PAR sensors or a single spectral band is not appropriate to derive accurate estimation of LCC or CCC. Alternatively, LCC estimations using RGB images was investigated in several studies (do Amaral et al., 2019; Guo et al., 2020; Sánchez-Sastre et al., 2020; Zheng et al., 2018). Although good correlations between RGB indices and LCC values were found, the empirical relationships were various and need to be calibrated depending on the experiment (Baresel et al., 2017; Rigon et al., 2016), limiting their applications in various locations autonomously.

Continuous and concurrent measurements of GAI, LCC and CCC require data from multiple spectral bands. Several automated field spectroscopy systems composed of high or ultra-high resolution spectrometers were developed to collect canopy reflectance and canopy sun-induced fluorescence signals (Campbell et al., 2019; Cogliati et al., 2015a; Grossmann et al., 2018a; Yang et al., 2018). However, these high-resolution spectrometers are designed for studying the SIF signal, which requires very accurate calibration and fine spectral resolution, with a cost ranging from 900$ to 8000$. Additionally, they are mounted on a tripod (Cogliati et al., 2015b) or towers (Campbell et al., 2019; Grossmann et al., 2018b; Yang et al., 2018), making them not practical when removing them for field management purposes. Therefore, the recent advances of low-cost and portable multi-band spectrometers provide an attractive option for assessing vegetation status by measuring the radiation reflected by the canopy autonomously in multiple wavebands ranging from visible to near infrared (NIR) (Fletcher and Fisher, 2018). The very low price of the sensor (e.g., less than 10$ from the manufacturer) makes it possible to put several systems in the field to better capture the spatial heterogeneity. Additionally, this type of device can be easily installed in the field without requiring any specific knowledge from the user. Despite these advantages, only few studies attempted to use these sensors (Garrity et al., 2010; Heusinkveld et al., 2023; Kim et al., 2022). Relatively few investigations have been devoted for simultaneous estimation of GAI, LCC and CCC from similar multi-band spectrometers, especially under natural environment. Unlike the experiments in laboratory with controlled environment, the varying illumination conditions (e.g., totally clear, sparse clouds or overcast) are inevitable in natural environment. They may have significant impact on the observations, and proper attention must be paid to possible calibration issues when using radiative transfer model or vegetation indices to retrieve canopy traits. Indeed, three crucial questions need to be solved when retrieving

variables under natural environments using multi-band spectrometer installed on a near-surface platform.

(1) Contribution of the direct and the diffuse component of the irradiance in each spectral band: retrieving vegetation variables from radiative model inversion requires to compute the reflectance (Fang et al., 2019; Jay et al., 2017; J. Wang et al., 2022). Natural irradiance is actually composed of a direct component and a diffuse component, which should be taken into account when using near-surface monitoring systems (Durand et al., 2021; Schaepman-Strub et al., 2006). Although some studies have investigated the partitioning of the radiation into its diffuse and direct components in the full solar domain, applicable with a reasonable accuracy everywhere at the Earth's surface (Gueymard and Ruiz-Arias, 2016; Yang and Gueymard, 2020), only few of them considered the PAR using data driven approaches calibrated on a single site experiment (Jacovides et al., 2010; Ma Lu et al., 2022; Spitters et al., 1986) or semi-empirical models (Oliphant and Stoy, 2018).

(2) Radiometric calibration: absolute radiometric calibration is a critical step to convert the radiance measured from spectrometer into reflectance, to limit the influence of changing illumination conditions. In the field, it can be achieved by performing radiance measurements over a Spectralon reference panel or a gray carpet with known reflectance placed close to the target (Cao et al., 2019; Li et al., 2021b; Peltoniemi et al., 2005; Sandmeier, 2000). However, this method is difficult to implement for continuous multi-band spectrometer monitoring in natural environments, because some calibration errors may be caused when the reference gets dirty and/or when its reflection properties change over time (Peltoniemi et al., 2005; Roosjen et al., 2017). When accurate radiometric calibration is not available, studies from Verger et al., (2014) and Jay et al., (2019) showed that using the ratio of the signal measured in a given band to the average of all measured bands or a single band, is an effective solution for retrieving vegetation variables.

(3) Diurnal variation of the sun position over the day: multiple sun viewing angles are available through continuous measurements in few minutes or hours steps. Many field instruments rely on the angular variations of the gap fraction either using the variation of the viewing or solar directions (Yan et al., 2019; Yin et al., 2017). This has also been investigated for multispectral observations from satellite and drones (Dorigo, 2012; Duan et al., 2014; Roosjen et al., 2018; Roujean and Lacaze, 2002; X. Zhang et al., 2021). But exploiting the dense diurnal sun variations of daily acquisitions using multi-band spectrometer has not been yet explored at our knowledge.

Under this context, the objective of this study is to find solutions to those three questions in order to develop a synthetic and practical algorithm to generate daily GAI, CCC and LCC from continuous ground measurements. We first present a method to partition the PAR incident radiation into its direct and diffuse component using a data driven approach. Then, we establish relationships between the diffuse fraction in the PAR domain and each spectral bands using the 6S radiative transfer model (Vermote et al., 1997). Then they were used in simulation of hemispherical-directional reflectance factor (HDRF) through a kernel-driven model (Roujean et al., 1992) and PROSAIL model (Jacquemoud et al., 2009). Both observations and simulations were converted into relative terms as a substitute of absolute radiometric calibration. Kernel parameters were calculated from the kernel-driven model and diurnal relative multi-band spectrometer measurements. The Artificial Neural Network (ANN) algorithm was employed to retrieve GAI, LCC and CCC from kernel parameters and geometric configurations. Using continuous multi-band spectrometer observations from IoTA (Internet of Things for Agriculture) systems over several wheat fields in France, we studied the robustness and accuracy of this algorithm. To evaluate the accuracy and uncertainties, we compared estimated diffuse fraction on each waveband, GAI, LCC and CCC with corresponding reference measurements.

2 Experiments and measurements

2.1 Study area

The experiments were conducted in 2019 in winter wheat fields of six areas close to the following French cities: Gréoux-les-Bains (43.75 °N, 5.88 °E), Nîmes (43.8 °N, 4.36 °E), Boigneville (48.3 °N 2.4 °E), Muizon (49.27 °N, 3.89 °E), Chalons-en-Champagne (49.0 °N, 4.4 °E) and Saint-Hilaire-en-Woëvre (49.1 °N, 5.7 °E) (Fig. 1). The Gréoux and Nîmes sites are characterized by a typical Mediterranean climate, with a maximum average temperature of 20 °C (Meteo France). The Boigneville site has a more continental climate, with maximum average temperature of 15 °C. In Muizon, Chalons-en-Champagne and Saint-Hilaire-en-Woëvre, the climate is temperate and humid and the maximum average annual temperature is around 13°C.

In total, 43 IoTA systems were installed (Table S1). Six of them were located in small experimental fields of 10 × 2 m² size where wheat was fertilized with different amounts of nitrogen. The remaining 37 sensors were installed in farm fields, with a size around 800 × 200 m². In the four northern sites, seven winter soft wheat (*Triticum aestivum*) cultivars were

grown. In the two southern sites, the fields were sown with three winter durum wheat (*Triticum durum*) cultivars. The sowing dates varied from end of October to beginning of November due to different planting practices and local weather. The IoTA measurement campaign started from the end of March (beginning of growth) to mid- May 2019 (maximum GAI) for most of the systems. Few of them were maintained on the field until the harvest date (Table S1). The systems were placed sufficiently far from the field border so that no border effect could impact the signal.

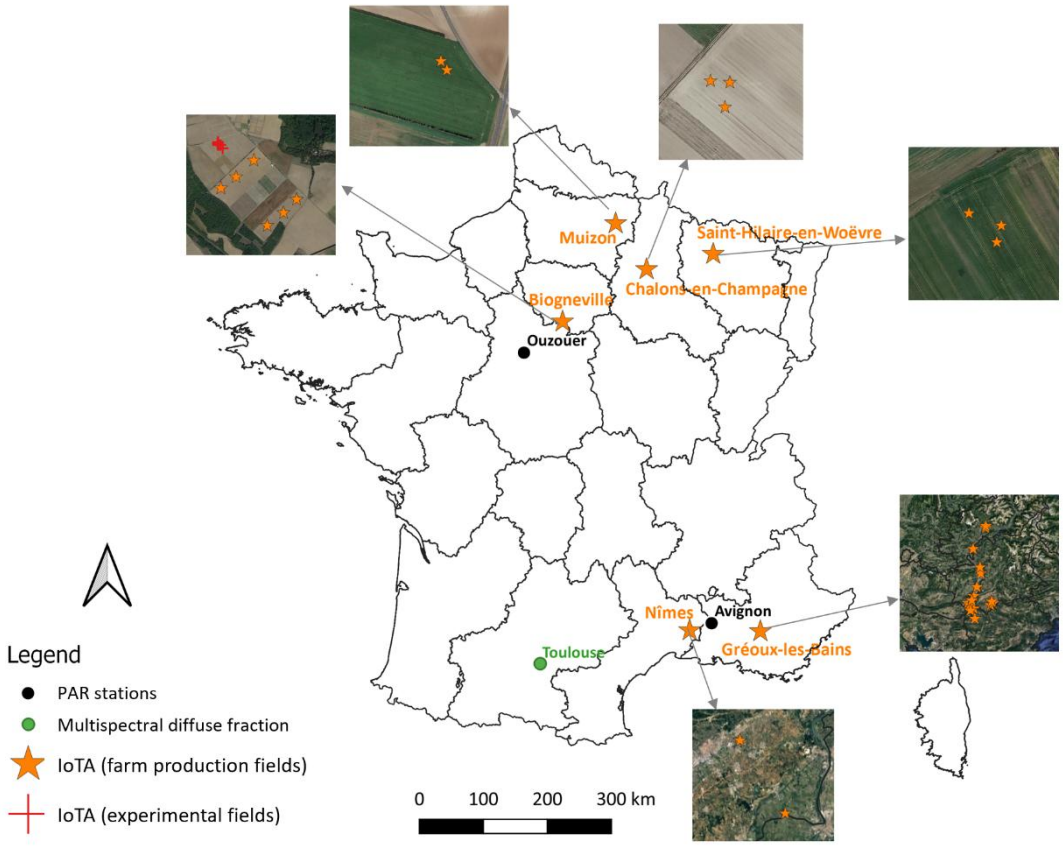

Fig. 1. The location of IoTA systems on production fields (orange stars) and experiment fields (red crosses), PAR measurements (black filled circles) and spectral diffuse fraction measurements (green filled circles) in 2019. Google Earth satellite were loaded from QGIS and they do not represent images during the measurements.

2.2 Ground measurements

2.2.1 IoTA systems

The IoTA system, developed by the HIPHEN and Bosch companies, is an autonomous system equipped with a miniature multispectral spectrometer, an upward looking

hemispherical PAR sensor, a meteorological sensor, as well as a RGB camera (Fig. 2a) (Velumani et al., 2020).It is powered by a battery that can provide continuous power support of 4 months. The multi-band spectrometer (AS7263 from AMS) is characterized by six wavebands, centered in the red (610 nm, 680 nm), red-edge (730 nm, 760 nm) and near infrared (810 nm, 860 nm) domains, with a full-width at half-maximum of 20 nm (Fig. 2b). More details about the spectrometer can be found in the producer website (https://ams.com/as7263).

The head of the IoTA was located 1.5 m above the ground, which roughly corresponded to a height of 0.5 m above canopy during the peak growth stage, (e.g., maximum height). It was oriented at a zenith angle of 45° from the vertical, with a $\pm$20° field of view to allow enough spatial sampling, and positioned so that the azimuth direction was perpendicular to the row in the field in order to maximize the amount of vegetation seen by the sensor (Baret et al., 2010). The PAR sensor points vertically upwards to measure the downward flux radiation. Canopy reflected radiation and downwelling PAR were measured simultaneously every 15 minutes during the whole campaign. The measurements were transferred automatically to a cloud storage system through a Global System for Mobile Communications (GSM) network.

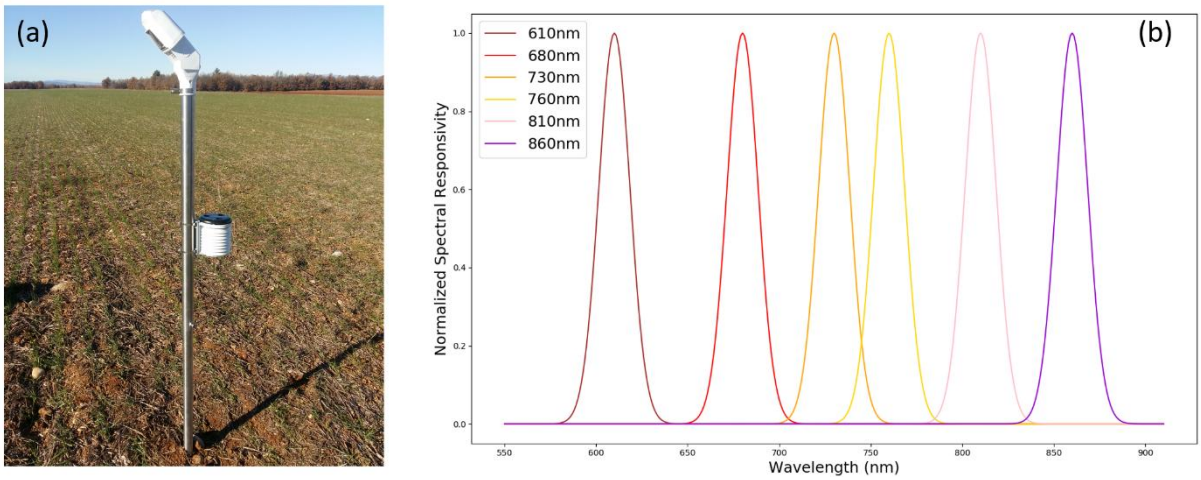

Fig. 2. (a) Illustration of an IoTA system installed in Gréoux (ID: FS-11, 43.797°N, 6.11°E, Table S1). The photo was taken at 12:37 on 11/12/2018. The head part inclined at 45° hosts the multi-band spectrometer and one RGB camera as described by Velumani et al., (2020) to monitor wheat phenology, in particular wheat heading. The cylinder box attached to the vertical pole was installed sensors to measure PAR, temperature and moisture. (b) Normalized spectral responsivity of each waveband of multispectral spectrometer.

2.2.2 PAR diffuse fraction

In this study, we used multi-year direct and diffuse PAR measurements acquired in meteorological weather stations located close to the experimental sites: Avignon (43.91 °N, 4.88 °E) near Gréoux-les-Bains and Nîmes, and Ouzouer (47.92 °N, 1.53 °E) near Boigneville (Fig. 1). Measurements were continuously acquired every 15 minutes with a BF3 sunshine sensor (Delta-T Devices Ltd, 2002). After removing outliers (negative values and diffuse PAR larger than total PAR), we kept 89116 valid measurements performed between 2001 and 2019 in the Avignon site and 10149 valid measurements performed in 2016 in the Ouzouer site. The PAR diffuse fraction was computed as the ratio of the diffuse PAR to the total PAR.

2.3 Validation datasets

2.3.1 Reference measurements of effective GAI, LCC and CCC

Reference effective GAI measurements were collected using downward-looking RGB cameras (Table S1) inclined at 45° zenith angle at around 1.5 m above the top of canopy, facing perpendicularly to the row. To maintain the 45° zenith direction during the acquisition, the cameras were mounted on a vertical monopod equipped with a spirit level. Three to five photos were taken in the area surrounding each IoTA system, which was considered sufficient regarding the strong homogeneity of the sampled area. Although the segmentation algorithm is robust against illumination conditions (Madec et al., 2023; Serouart et al., 2022), all photos were taken between 10 am to 3 pm local time in order to reduce possible shadow impacts.

GAI was then estimated after applying a semantic segmentation to the images in order to separate the green vegetation from the background and inverting the Poisson model that relates the gap fraction GF in a direction θ to GAI:

$$GF(\theta) = exp\left(-\frac{G(\theta_l,\theta).GAI}{\cos(\theta)}\right) \quad (1)$$

Where θ is the view zenith angle, θ_l is the average leaf inclination angle, and $G(\theta_l, \theta)$ is the mean projection of a unit foliage area. We used the same methodology as Baret et al. (2010) who took advantage of a view zenith direction at 57.5° to get a direct gap fraction-GAI relationship which is independent of the leaf inclination (Weiss et al., 2004). However, for such high viewing angles, it is difficult to obtain accurate classification results for dense canopies (GAI > 3) due to some saturation effects which prevent from discriminating accurately the green material from the background. Therefore, a lower viewing angle of 45° was preferred as it eases the image segmentation and still allows assuming that the G-function

is almost constant for wheat. Indeed, although wheat cultivars may present a range of leaf inclination types between erectophile and planophile depending on the phenological stage, the overall green material inclination (e.g. culms) was demonstrated to be erectophile (from 70° to 80°), by Barillot et al. (2019). For this specific range, Fig. 3 shows that $G(\theta_l, \theta)$ can be assumed constant (G-slope = -0.0013).

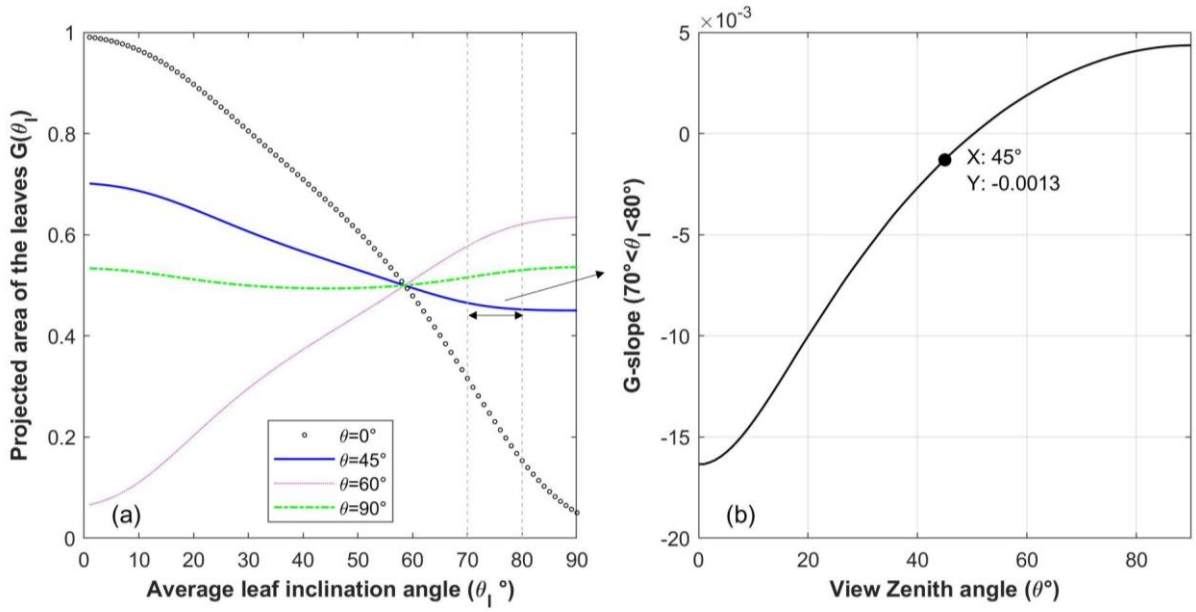

Fig. 3. (a): Variation of the mean projection of the unit foliage area (G-function) with the average leaf inclination (assuming an ellipsoidal leaf inclination distribution). (b): Slope of the G-function for erectophile canopies ($70° < \theta_l < 80°$) as a function of the view zenith angle θ.

The semantic segmentation of the gap fraction images relies on a deep learning approach developed on wheat and described and evaluated by Serouart et al. (2022). This method was composed of two steps. A U-net model was first trained over a large dataset to separate vegetation from background. Then, a support vector machine was used to classify the vegetation masks into green and non-green components. The training dataset of each step is independent using wheat at different phenological stages in a variety of environments and under different illuminations. The gap fraction of each RGB image was calculated as the ratio of the number of non-green pixels to the total number of pixels in the image. The RGB images used to derive the GAI were cropped so that the original vertical field of view was restricted to 45° ± 5° to meet the constant-G assumption while ensuring enough spatial sampling while the original horizontal field of view was restricted to ± 20° to meet the IoTA

characteristics (examples were shown in Fig. S1). This allowed us to remove blurred objects at the border of image when the distance of the sensor to the vegetation is large. By considering the image cropping in this study, we finally computed the equivalent coefficient to derive GAI from the gap fraction (Eq. (3)), the latter being obtained from the segmented cropped image as the ratio between the number of background pixels and the cropped image size:

$$\boldsymbol{GAI} = -\frac{\boldsymbol{cos\theta}}{\boldsymbol{G(\theta_l,\theta)}}\boldsymbol{ln(GF(\theta))} \quad (2)$$

For θ_l between 70° and 80°, and view zenith angle θ between 40° and 50°(camera inclination angle is 45° and we crop the images from the center to ±5°), Eq. (2) is reformulated as:

$$\boldsymbol{GAI} = -\frac{\boldsymbol{1}}{\boldsymbol{\int_{70}^{80}\int_{40}^{50}\frac{G(\theta_l,\theta)}{cos\theta}d\theta d\theta_l}}\boldsymbol{ln(GF(\theta))}, \text{ where } \boldsymbol{\int_{70}^{80}\int_{40}^{50}\frac{G(\theta_l,\theta)}{cos\theta}d\theta d\theta_l = 0.65} \quad (3)$$

GAI of each image was computed and mean value was used in the validation.

The leaf chlorophyll content was measured using the SPAD device (Minolta, 2009) with a minimum of 15 leaves randomly located at the top of the canopy per sample within the field of view of the IoTA during March 28 to June 18 in 2019. The SPAD measurement dates were different among fields, but generally every 10 to 20 days on key growth stages. These SPAD raw readings should be converted into content of chlorophyll (μg/cm^2) using relationships with absolute LCC measured in laboratory. Since there was no absolute LCC measurement in this study, we proposed an ensemble method to compute the reference. First, we applied multiple equations in literatures (Table S2) to convert our SPAD readings to LCC. Then the median of all LCC from single SPAD reading was computed as reference to validate corresponding IoTA retrieval. The standard deviation of LCC from different equations was used as the uncertainty of the reference dataset. Only equations built with only wheat dataset or including wheat were selected. The total canopy chlorophyll content (g/m^2) was then obtained by multiplying the GAI and the LCC that were measured within three days.

2.3.2 Reference measurements of multispectral camera diffuse fraction

One important step of the algorithm is to estimate spectral diffuse fraction from IoTA PAR measurements. We therefore used a multispectral sensor with band settings similar to multi-band spectrometer to validate the accuracy of spectral diffuse fraction estimations. A specific experiment was designed and conducted at the INRAE site of Toulouse (43.53 °N,

1.50 °E) from the 31st July 2019 to 1st August 2019 (Lopez-Lozano et al., 2019). That period corresponded to a changeable weather with various illumination conditions induced by moving clouds during the whole morning on both dates. Measurements were acquired with the AIRPHEN multispectral camera (https://www.hiphen-plant.com/solutions/airphen/) which has six synchronized multispectral bands centered at 450 nm, 530 nm, 570 nm, 675 nm, 730 nm and 850 nm, with a full width at half maximum close to 10 nm (Li et al., 2021a), and thus present some similarities with the IoTA systems (Fig. 2). More details about the experiment are presented in Supplementary Materials Part B (Fig. S2, Table S3).

3 Methods

Our approach is split in three steps (Fig. 4): 1) estimation of the PAR diffuse fraction; 2) the estimation of the spectral diffuse fraction in each IoTA band; and 3) the estimation of daily GAI, LCC and CCC variables.

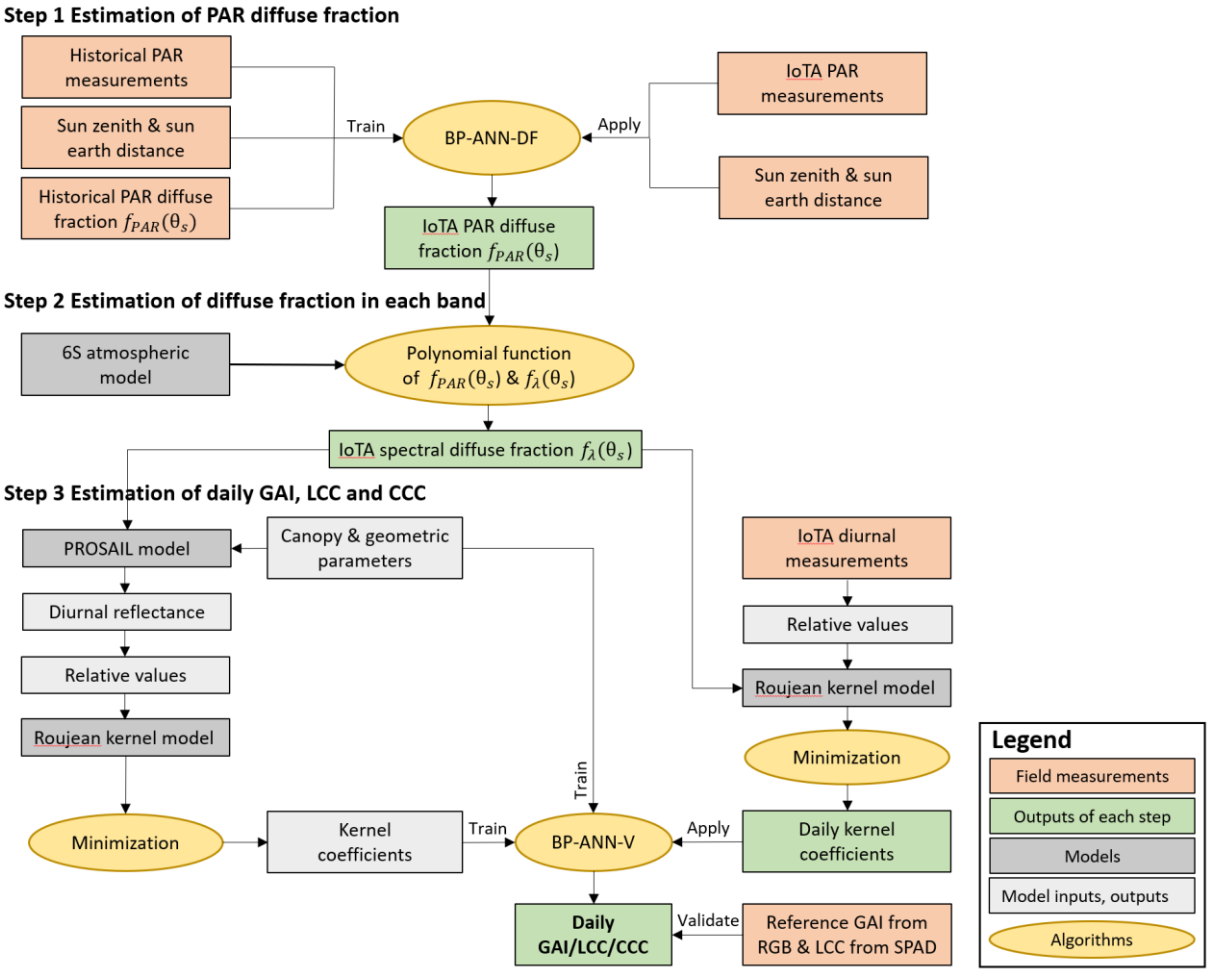

Fig. 4. Flowchart of retrieving daily GAI, LCC and CCC from IoTA measurements.

3.1 Step 1: Estimation of PAR diffuse fraction f_{PAR}

We first trained a neural network to directly estimate the PAR diffuse fraction using the ground total PAR (PAR_T) measured by each IoTA without considering ancillary inputs. Similarly to Jacovides et al. (2010) who related global and diffuse PAR by fitting empirical functions, we used PAR_T as input and we complemented by the cosine of the sun zenith angle and the sun-Earth distance correction coefficient $d(t)$ at each acquisition date (Spitters et al., 1986). $d(t)$ is derived as

$$d(t) = \frac{1}{(1-0.01673\times\cos(0.0172\times(t-2)))^2} \quad (4)$$

where t is the Julian day corresponding to the acquisition date with reference of 01/01/1950. Indeed, adding $d(t)$ as input improves the accuracy of estimation.

We used ground measurements of the instantaneous total and diffuse PAR acquired over multiple years described in Section 2.2.2 to generate the training database. The inputs included instantaneous total PAR, $d(t)$ and optical path defined as the cosine of sun zenith angle, and the output was the instantaneous diffuse PAR. The database has in total 84587 cases, and it was divided into two parts: 69659 samples were randomly selected to train the neural network, and the remaining 14928 samples were used for overfitting control and evaluation of the theoretical performances.

We found that a Back Propagation Artificial Neural Network (BP-ANN) made of one hidden layer of four neurons characterized by a tangent-sigmoid transfer function followed by a single linear transfer function output neuron provided the best results, e.g., no overfitting and best accuracy. Ten BP-ANN-DF were trained and the performance using the training dataset was shown in Fig. S3. The best one was selected based on the smallest root mean square error (RMSE) computed on the validation dataset. It was then applied to instantaneous PAR measured by each IoTA to estimate corresponding PAR diffuse fraction.

3.2 Step 2: Estimation of the diffuse fraction in each band f_λ

Step 2 consists in retrieving the diffuse fraction in each band f_λ from the PAR diffuse fraction estimated in step 1 (section 3.1). Based on the study by Spitters et al. (1986), we first isolated fully cloudy conditions and the other conditions. When $f_{PAR}$is greater than 0.9 (e.g. cloudy conditions), f_λ is assumed to be equal to f_{PAR}; otherwise, the diffuse fraction in each band was estimated by using a polynomial function calibrated using simulations of 6S atmospheric correction model (Vermote et al., 1997).

Using 6S (version v2.1), we simulated the variation of the diffuse fraction by considering a range of aerosol optical thicknesses (e.g., visibility ranging from 1 km to 40 km by steps of 2 km). We assumed a continental aerosol model that fits with the atmospheric characteristics of our areas of interest. For each sun zenith angle ranging from 20° to 65° with a step of 5°, we simulated the direct and diffuse absolute irradiance over 400 – 900 nm and accounted for the spectral response function of each spectral band (e.g., of the IoTA or the AIRPHEN camera) to simulate the corresponding $\boldsymbol{f}_{\boldsymbol{\lambda}}$. Similarly, direct and diffuse PAR and corresponding $\boldsymbol{f}_{PAR}$ were computed by integration over the 400 - 700 nm range. We then fitted a five-degree polynomial between $\boldsymbol{f}_{PAR}$ and $\boldsymbol{f}_{\boldsymbol{\lambda}}$ that we applied when $\boldsymbol{f}_{PAR}$ is lower than 0.9 (Table S3).

3.3 Step 3: Estimation of daily GAI, LCC and CCC

3.3.1 Generation of PROSAIL training database

Similarly to Li et al., (2015) and Weiss et al., (2020), a training database was simulated thanks to the PROSAIL radiative transfer model that couples PROSPECT (Jacquemoud and Baret, 1990) to simulate the leaf optical properties and SAIL (Verhoef, 1985, 1984) to generate top of canopy reflectance. Table 1 lists the range and distribution law for all variables of PROSAIL model. The soil reflectance data was simulated using five typical soil reflectance spectra multiplied by a brightness coefficient allowing to increase the diversity in actual soil properties (Weiss et al., 2020). This resulted in a total of 41472 combinations of canopy structures, leaf biophysical properties and backgrounds. For every combination, the hemispherical-directional reflectance $\rho_{HDR,\lambda}(\theta_s, \theta_v, \phi)$ and bi-directional reflectance $\rho_{BRDF,\lambda}(\theta_s, \theta_v, \phi)$ at waveband λ (Schaepman-Strub et al., 2006) were computed for any sun-sensor geometry, defined by the sun zenith angle θ_s, the view zenith angle θ_v and the relative sun-sensor azimuth angle ϕ. To consider the multiplicative or additive uncertainties of measured reflectance and get a more realistic canopy reflectance simulated value, an uncertainty model was used to describe the additive and multiplicative uncertainties based on a white Gaussian noise as previous studies (Li et al., 2015; Weiss et al., 2020).

To increase the realism of the distribution of f_{λ}, we relied on the IoTA measurements of the PAR diffuse fraction and sun positions to well sample the actual conditions of illuminations. From all available instantaneous real measurements, we totally extracted 2080 daily combinations and each combination includes several instantaneous f_{λ}, corresponding sun zenith angle and relative azimuth angles during one day. Since the sampling interval of

acquisition is 15 minutes, each daily combination has at least 20 sets of instantaneous f_λ, corresponding sun zenith angle and relative azimuth angles, after removing outliers (e.g., negative f_λ, or $f_\lambda > 1$, or sun zenith angles larger than 60°). The 2080 combinations were repeated to a total size of 41472, randomly sorted. To note, the data in each combination don't change. Then, they were combined with each of 41472 cases generated with the other PROSAIL inputs. Finally, each simulation case is composed of variables for canopy structures, leaf biophysical properties, backgrounds and a set of instantaneous f_λ, corresponding sun zenith angle and relative azimuth angles.

Table 1. List of variables and corresponding distribution laws to run the PROSAIL simulations. Distribution laws are described by their mean and standard deviation (Std). ALA = Average Leaf Angle inclination; HOT = Hot-spot parameter; N = leaf structure parameter; Cdm = dry matter content; Cw_Rel = relative leaf water content; Cbp = brown pigment concentration; Bs = soil brightness.

	Variable	Minimum	Maximum	Law	Mean	Std
Canopy	GAI	0.0	7.0	Gauss	2.0	2.0
	ALA (°)	60	80	Gauss	70	20
	HOT	0.1	0.5	Gauss	0.2	0.5
Leaf	N	1.20	1.80	Gauss	1.50	0.30
	Cab (µg.m^{-2})	20	80	Gauss	40	10
	Cdm (g.m^{-2})	0.003	0.011	Gauss	0.005	0.005
	Cw_Rel	0.60	0.85	Uniform	0.75	0.08
	Cbp	0.00	2.00	Gauss	0.00	0.30
Soil	Bs	0.50	3.50	Gauss	1.20	2.00

3.3.2 Setting up the neural network (BP-ANN-V) for GAI, CCC and LCC estimation

Because practical considerations to make the use of reference panels are not available and the incoming irradiance is unknown, we cannot perform absolute calibration of the IoTA spectrometer to derive reflectance values as simulated by PROSAIL. Therefore, we used the ratio between the signal in a given band to the mean value over all bands according to Verger et al. (2014):

$$\overline{X_\lambda(\theta_s,\theta_v,\phi)} = \frac{X_\lambda(\theta_s,\theta_v,\phi)}{\sum_{\lambda=1}^{6} X_\lambda(\theta_s,\theta_v,\phi)/6} \quad (5)$$

where $X_\lambda(\theta_s,\theta_v,\phi)$ is either the irradiance $R_\lambda(\theta_s,\theta_v,\phi)$ measured by the IoTA spectrometer at waveband λ, at sun zenith angle θ_s, view zenith angle θ_v and relative sun-sensor azimuth angle ϕ, or the reflectance $\rho_\lambda(\theta_s,\theta_v,\phi)$ simulated by PROSAIL. $\overline{X_\lambda(\theta_s,\theta_v,\phi)}$ represents the relative correspondence.

Due to operational constraints and computational costs, the inversion of the PROSAIL model is performed by training a machine learning algorithm as it is currently done in the remote sensing community (Verrelst et al., 2012). The machine learning algorithm must make use of the IoTA signal and sun geometry as inputs and the variable of interest (GAI, LCC and CCC) as output. Assuming that these variables are constant during a whole day, the whole set of 15 min acquisitions composed of six spectral bands and three angles varying from day to day, can be exploited for a single retrieval. This makes a huge set of inputs with strong correlations, suggesting to apply dimensionality reduction (May et al., 2011). Therefore, similarly to Weiss and Baret (1999), we used kernel driven BRDF models (Roujean et al., 1992) to reduce the dimensionality of the directional information. However, conversely to Weiss and Baret (1999) that was performed on satellite data, we needed to account for the contribution of the direct and diffuse components and used a modified version of kernel BRDF models (Dong et al., 2018).

The modeled $X_\lambda(\theta_s,\theta_v,\phi)$, denoted $X_{mod,\lambda}(\theta_s,\theta_v,\phi)$, is expressed as the sum of the diffuse and the direct contributions:

$$X_{mod,\lambda}(\theta_s,\theta_v,\phi) = f_\lambda(\theta_s).X_{HDR,\lambda}(\theta_v) + [1 - f_\lambda(\theta_s)].X_{BRDF,\lambda}(\theta_s,\theta_v,\phi) \quad (6)$$

where $X_{HDR,\lambda}(\theta_v)$ and $X_{BRDF,\lambda}(\theta_s,\theta_v,\phi)$ are, respectively, the canopy hemispherical-directional component and canopy bi-directional component (Schaepman-Strub et al., 2006), and $f_\lambda(\theta_s)$ is the diffuse fraction at wavelength λ and sun zenith angle θ_s. According to Dong et al. (2018), $X_{mod,\lambda}(\theta_s,\theta_v,\phi)$ in Eq. (6) can be simulated from a revised kernel-driven model :

$$X_{mod,\lambda}(\theta_s,\theta_v,\phi) = f_{iso,\lambda} + f_{vol,\lambda}K_{volDLC,\lambda}(\theta_s,\theta_v,\phi) + f_{geo,\lambda}K_{geoDLC,\lambda}(\theta_s,\theta_v,\phi) \quad (7)$$

where $K_{volDLC,\lambda}$ and $K_{geoDLC,\lambda}$ are diffuse-light correction (DLC) versions of original kernels of $K_{vol,\lambda}$ and $K_{geo,\lambda}$ present in Roujean et al. (1992). The DLC kernels are the sum of original kernels and their integrals over the illumination hemisphere weighted by $f_\lambda(\theta_s)$(Dong et al., 2018). $f_{vol,\lambda}$ and $f_{geo,\lambda}$ are, respectively, the coefficients of the $K_{volDLC,\lambda}$ and $K_{geoDLC,\lambda}$ (Roujean et al., 1992).

For either PROSAIL reflectance simulations or IoTA measurements, 18 kernel coefficients (three kernels times six bands) were estimated from a series of acquisitions or simulations by minimizing the following cost function:

$$J\left[\left(f_{iso,\lambda}, f_{geo,\lambda}, f_{vol,\lambda}\right)_{\lambda=1\ldots6}\right] = \sum_{\theta_s,\theta_v,\phi} \sum_{\lambda=1}^{6} \left[\overline{X_\lambda(\theta_s,\theta_v,\phi)} - \overline{X_{mod,\lambda}(\theta_s,\theta_v,\phi)}\right]^2 \quad (8)$$

where $\overline{X_{mod,\lambda}(\theta_s,\theta_v,\phi)}$ is the relative values obtained by combining Eq. 5 and Eq. 7. The cost function J was minimized using Sequential Least SQuares Programming algorithm (Kraft, 1988).

In the case of PROSAIL reflectance simulations, kernel coefficients were estimated for each case of the 41472 simulations that corresponds to a given set of acquisitions. In the case of IoTA, only instantaneous measurements with sun zenith angle less than 60°, f_{PAR} is positive and lower than 1 and measurements are positive were treated as valid and used in the estimation of kernel coefficients. Since the optimization algorithm requires at least 18 measurements for the estimation of 18 coefficients (3 kernel coefficients × 6 wavelengths) at the same time, IoTA daily continuous observations acquired during a moving window of 1, 3, 5 or 7 days were used, assuming that the crop variables remain stable during this short period. The sensitivity of kernel parameter estimation to the size of moving window was evaluated by computing the RMSE between simulations from kernel parameters and real IoTA measurements.

3.3.3 Training and applying the BP-ANN-V

Following Weiss and Baret (1999) and Li et al. (2015), we trained one BP-ANN-V per each variable. The training database was divided into two parts: two thirds of the simulations were randomly selected to train the neural network and the remaining one third was used for validation. The inputs were the 18 kernel parameters, and the output was either GAI, LCC or CCC. Each neural network was made of one input layer, one hidden layer composed of 5 neurons with tangent sigmoid transfer functions and one output layer with a linear transfer function. For each output variable, ten networks were trained with different initial guess of the weight. They were applied to kernel parameters derived from diurnal IoTA measurements and the median of inversions from ten networks was computed as the final result, which allows better generalization capacities.

We kept only field measurements for which the BP-ANN-V estimates are within a given range described in (Table 2) and that the kernel parameters obtained from the IoTA systems fall within the range of those obtained from the PROSAIL simulations.

Table 2. The minimum, maximum values and tolerance for each output product.

	Unit	Minimum	Maximum
GAI	m^2/m^2	0	7
LCC	$\mu g/cm^2$	0	80
CCC	g/m^2	0	5.6

3.4 Evaluation procedures

Model accuracy was assessed thanks to different statistics: coefficient of determination (R^2), bias and root mean squared error (RMSE), Relative bias which is the ratio between bias and average of reference, and relative RMSE which is the ratio of RMSE to average of references are also computed to provide further evaluation information.

4 Results

4.1 Diffuse fraction from incoming PAR measurements

4.1.1 PAR diffuse fraction

The results presented in Fig. 5 show that, over our experimental sites, the PAR diffuse fraction can be accurately estimated from the total PAR, sun zenith angle and a correction coefficient accounting for variations in sun-Earth distance, using the BP-ANN-DF neural network (R^2 = 0.86, RMSE = 0.11). Our dataset mainly includes low diffuse fraction values (lower than 0.5), mostly corresponding to the Avignon site in Southern France characterized by frequent sunny illumination conditions and small aerosol concentration values, and very high diffuse fraction values (greater than 0.9), mostly corresponding to the Ouzouer site in Northern France which presents frequent overcast illumination conditions. Additional medium PAR diffuse fraction measurements might thus be required to ensure a similar accuracy over the intermediate range of values.

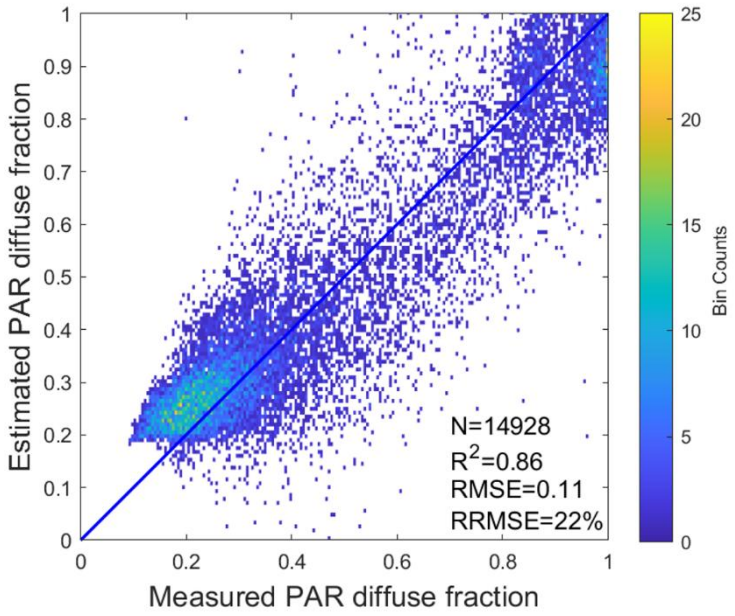

Fig. 5. Performances of PAR diffuse fraction estimation from neural networks (BP-ANN-DF) over the validation dataset (Avignon-Ouzouer measurements). Colors correspond to the number of data available for a given f_{PAR} value.

4.1.2 Spectral diffuse fraction

The relationship between f_{PAR} and f_λ was evaluated both using 6S model simulations in IoTA and AIRPHEN spectral bands, and using AIRPHEN camera ground measurements. Results from the 6S model simulations show that the f_λ is related to f_{PAR} through a polynomial relationship for IoTA (Fig. 6a) and the AIRPHEN camera (Fig. 6b). Under high to medium visibility conditions (e.g., $f_{PAR} < 0.9$), the PAR diffuse fraction is systematically higher than f_λ for the red to NIR domain and the difference increases with the wavelength due to the decreasing influence of aerosol effects. Accordingly, the PAR diffuse fraction is lower than $f_{\lambda 450nm}$ and is close to that at in the green wavelengths (530 nm and 570 nm). Under very low visibility sky conditions (e.g., $f_{PAR} \geq 0.9$), f_λ is almost equal to the PAR diffuse fraction for all the bands. We evaluated the fitted polynomial functions derived from 6S simulations using ground measurements acquired with the AIRPHEN camera (Fig. 6c). The spectral diffuse fractions were estimated with R^2 = 0.71, RMSE = 0.08 and relative RMSE = 29.57% (Fig. 6c) for all the six bands together, using the polynomial relationships presented in Table S3. The validation performance in each band was shown in Table 3. In general, all bands have good correlations with references ($R^2 \geqslant 0.83$ and RMSE $\leqslant 0.11$).

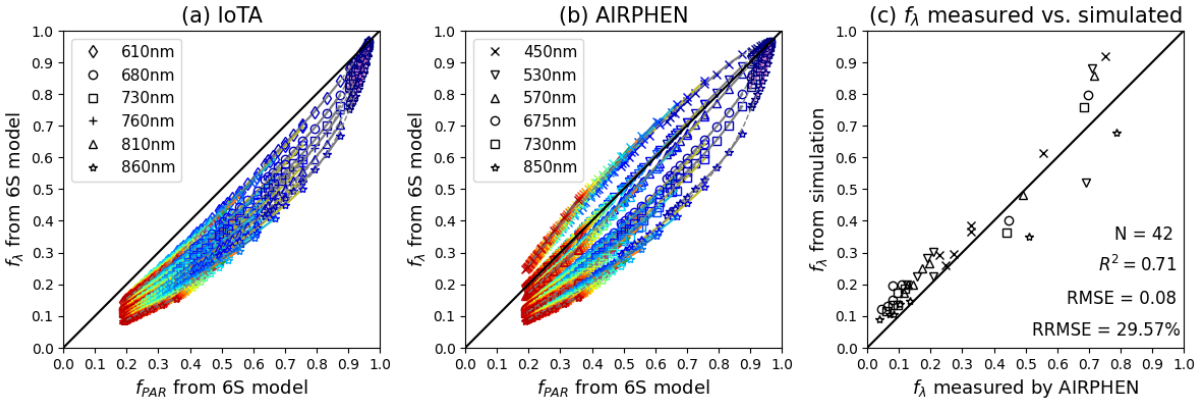

Fig. 6. Comparison between PAR diffuse fraction (f_{PAR}) and spectral diffuse fraction (f_λ) obtained from 6S model simulations for (a) the IoTA spectral bands and (b) the AIRPHEN camera bands. Different colors represent the visibility input to 6S model, while gray lines show the fitted polynomial relationships. (c) Spectral diffuse fractions estimated from polynomial relationships versus the ones measured by the AIRPHEN camera using PAR diffuse fraction of 0.9 as the threshold value to discriminate the cloudy conditions. R^2, RMSE and RRMSE were computed over all bands. RRMSE is relative RMSE calculated as the ratio between RMSE and average value.

Table 3. Statistics of comparison between simulated f_λ and measured f_λ of each wavelength of AIRPHEN camera. RRMSE is relative RMSE calculated as the ratio between RMSE and average of references.

	450 nm	530 nm	570 nm	675 nm	730 nm	850 nm
R^2	0.99	0.83	0.97	0.96	0.95	0.97
RMSE	0.08	0.11	0.08	0.08	0.06	0.08
RRMSE (%)	19.63	33.73	27.87	38.52	28.64	31.70

4.2 Suitability of kernel BRDF model parameters to be used as inputs to BP-ANN-V

We first retrieved the kernel BRDF model parameters in each spectral band and then reconstructed the corresponding relative reflectances that were compared to the initial relative reflectances simulated with PROSAIL. Results were very consistent with R^2 = 0.99 and an overall relative RMSE = 0.32% over all the wavelengths (Fig. S6). For each individual wavelength, a very good correspondence was also observed (Table 4). The performance was better on red-edge and NIR bands (relative RMSE < 1%), compared to the red bands (relative

RMSE > 1%). This indicates the kernel parameters can reconstructed the reflectance from PROSAIL model, thus can replace the reflectance from PROSAIL model in the inversion of biophysical variables. It also implies the good performance of the optimization methods applied on kernel-driven models.

Table 4. Statistics between relative reflectances ($\bar{\rho}$) obtained from PROSAIL simulations and reconstructed after BRDF kernel model inversion for each IoTA spectral band.

	610 nm	680 nm	730 nm	760 nm	810 nm	860 nm
R^2	0.999	0.999	0.999	0.999	0.999	0.999
RMSE	0.004	0.005	0.003	0.003	0.004	0.005
RRMSE (%)	1.87	1.11	0.35	0.21	0.23	0.32

The same exercise was applied to the IoTA measurements: we estimated the kernel BRDF model parameters using each set of measurements determined by the size of the moving window used (1, 3, 5, or 7 days). Like the regression in Fig. S6, the kernel model simulations also correspond very well with the measurements from IoTA relative measurements (R^2 > 0.98). The regression figure was therefore not shown for the sake of brevity. In order to further evaluate the performance of the optimization algorithm, we calculated the RMSE and used it to set a strict criterion to remove some outliers and select the best moving window size. The RMSE between kernel model simulated relative values and IoTA relative measurements over all bands ranges from 0 to 0.17 depending on the window size (Fig. 7). The median RMSE (0.009 – 0.014 in Fig. S7) was obviously larger than the 0.005 RMSE from PROSAIL model simulations because of the noise associated to the ground measurements. Although one white noise was added in the PROSAIL absolute reflectance, there are no quantitative results demonstrating the propagated uncertainties that includes all potential noises in the field, e.g., the diffuse fraction estimation, spectrometer intra-calibration among bands and noise co-distributions between bands.

The choice of the size of the moving windows is a compromise between the number of acquisitions used to retrieve the BRDF kernel parameters and the length of the window during which the canopy biophysical variable is assumed constant. When the window size increases from 1-day to 7-day, the number of acquisitions that could be used in the estimations almost doubles (Fig. 7a). The performance of kernel BRDF model inversion also varies with the number of acquisitions (Fig. 7b). When using a single day of acquisition, the RMSE fluctuates with a median RMSE of 0.014 (Fig. S7). Adding more measurements as inputs to

the optimization algorithm is helpful to find the local minimum. These results are improved when increasing the length of the moving window with very similar RMSE of 0.009 between 3-, 5- or 7-day window size. We therefore selected the 3-day window as the best compromise between accuracy and the assumption that GAI, CCC and LCC remain constant during that period.

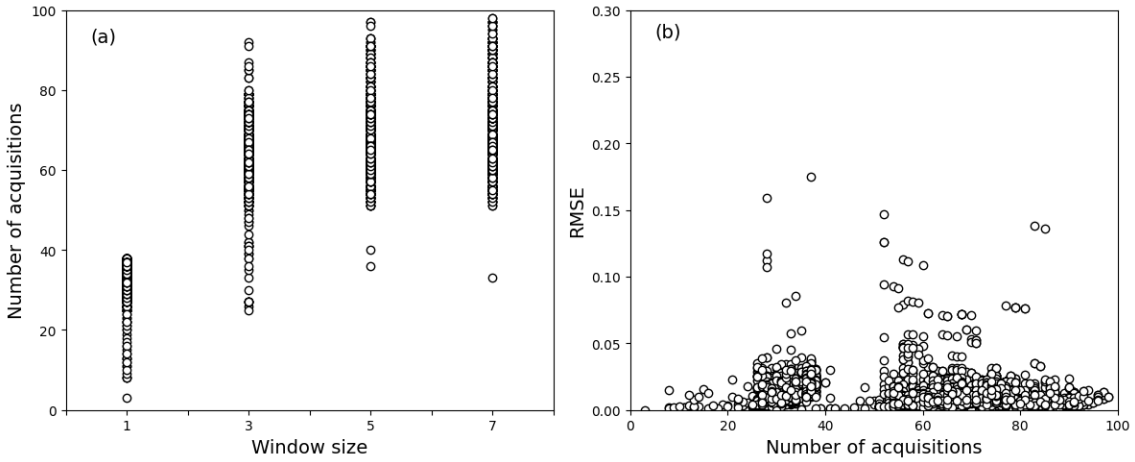

Fig. 7. (a) Number of IoTA acquisitions for each moving window size of 1, 3, 5, and 7 days; (b) Relationship between number of acquisitions with the RMSE calculated between the measured relative signal and kernel model reconstructed relative signal using moving window size of 1, 3, 5, and 7 days for the IoTA systems during the experiment campaign.

4.3 Validation against ground measurements

The retrieved biophysical variables were compared with the corresponding ground measurements at the same dates. The GAI estimated from IoTA systems has a very good consistency with the field data taken by RGB cameras (R^2 = 0.86, RMSE = 0.54, relative RMSE = 26.95%, Fig. 8a).

The LCC retrieval from IoTA has very similar correspondences with reference LCC converted using various equations (R^2 = 0.51 – 0.53) but quite different scattering and biases (RMSE = 5.59 µg/cm^2 – 18.94 µg/cm^2, relative RMSE = 12.08% - 65.51%) (Fig. S8). The best correlation and minimum RMSE was obtained using calibration equation No. 4 and 12, while the largest RMSE was found using equation No. 6. Using proposed ensemble method which took the median of all equations as the reference, IoTA LCC exhibits a good correlation but a systematic overestimation (R^2 = 0.52, RMSE = 12.06 µg/cm^2, relative RMSE = 33.34%) (Fig. 8b). The uncertainty of reference LCC ranges from 4.21 µg/cm^2 to 11.78 µg/cm^2, and the overall uncertainty is 7.44 µg/cm^2.

Conversely to LCC, the chlorophyll content at canopy level presents a good correspondence between ground reference datasets and estimations from IoTA systems (R^2 = 0.93, RMSE = 0.25 g/m^2, relative RMSE = 26.12%, Fig. 8c). Since the RGB images and SPAD measurements were taken on different dates and sites, only few measurements can be used to calculate the ground CCC values. In this study, we used the SPAD LCC and RGB GAI values measured within 3 days to compute CCC, assuming wheat status was stable during this period. This assumption is consistent with 3-day moving in the proposed algorithm (section 3.3).

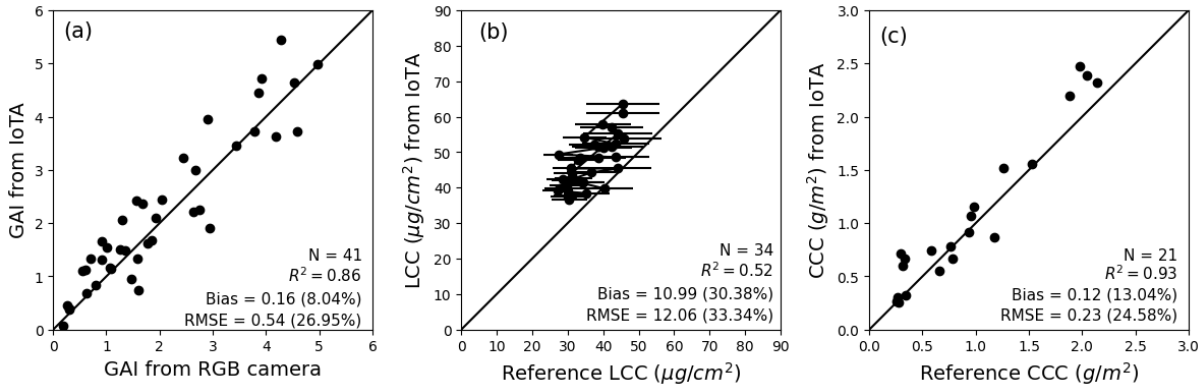

Fig. 8. Direct validation of (a) GAI, (b) leaf chlorophyll content and (c) canopy chlorophyll content derived from IoTA with the ground validation dataset. The dark line is the 1:1 line. In (b), error bars represent the standard deviation of LCC converted from all equations shown in Table S2. In (c), ground CCC was calculated from chlorophyll meter derived LCC and RGB camera derived GAI within 3 days assuming wheat status was stable during this short period.

When calculating relative values of IoTA measurements or PROSAIL simulations ($\overline{X_\lambda(\theta_s, \theta_v, \phi)}$), we used the average of all bands as denominator (Eq. (4)), as Verger et al. (2014) using multispectral camera onboard a drone. However, Jay et al. (2019) used 850 nm band of AIRPHEN camera as the denominator to compute relative values. Regarding to IoTA systems, we compared the inverted GAI, LCC and CCC from different relative values using average or single band as reference with ground measurements (Table 5). Results show that the performances are similar for GAI, R^2 ranging from 0.83 to 0.86. The differences are slightly larger for LCC, that using 810 nm and 860 nm as reference has the lowest correspondence (R^2 is around 0.4 to 0.42). For CCC, using average of all bands or 610 nm or 680 nm has similar better accuracy. Overall, using average of all bands as reference has best performance for the three variables in this study.

638 Table 5. Comparison of direct validation accuracy of GAI, LCC and CCC, estimated from
639 relative measurements using reference of mean of all bands and each single band.

Reference to compute relative values (nm)	GAI		LCC		CCC	
	R^2	RMSE	R^2	RMSE	R^2	RMSE
Average	0.86	0.51	0.52	8.44	0.93	0.25
610	0.85	0.56	0.47	9.52	0.91	0.26
680	0.83	0.58	0.47	8.74	0.91	0.26
730	0.83	0.56	0.48	9.02	0.79	0.32
760	0.85	0.55	0.52	9.72	0.8	0.31
810	0.83	0.55	0.4	9.73	0.8	0.33
860	0.83	0.59	0.42	10.53	0.78	0.34

640

641 ### 4.4 Continuous monitoring of GAI, LCC and CCC with IoTA systems

642 Temporal profiles of GAI, LCC and CCC over four sample sites are shown in Fig. 9.
643 Results show that the profiles capture well the expected seasonal variation of each variable.
644 Differences of GAI trends are observed among sites on the maximum values and the peak
645 growth period, for example, maximum GAI around 5 of AC-2 arrives on mid of May, while
646 the GAI of Fourques-1 and FS-3 sites increases from the beginning of April to a peak value of
647 4 in beginning of May. These differences among sites are mainly due to wheat variety,
648 climate, management practices and available measurement periods (Table S1). LCC also
649 presents seasonal variations although the data intervals are narrow, ranging from 40 to 80
650 µg/cm^2 over four sample sites. CCC which is the combination of GAI and LCC, presents
651 similar seasonal trends as GAI. Some fluctuations can be found over the three variables and
652 four sample sites, and the other sites which are not shown for brevity. They mainly result
653 from the availability of measurements during a day and inevitable error propagation of all
654 processing procedures. This is particularly obvious for CCC, because fluctuations of GAI and
655 LCC will be amplified in CCC after multiplication.
656

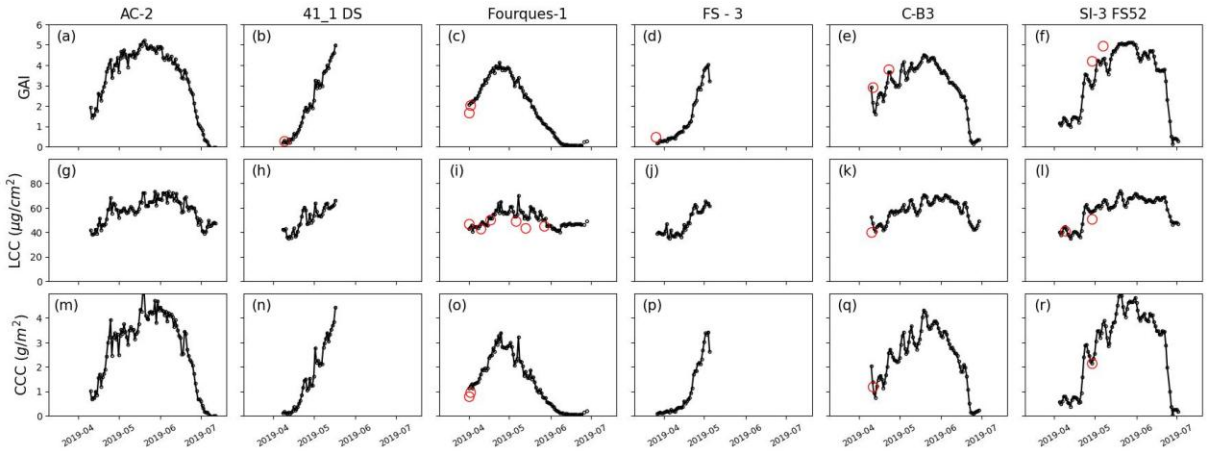

Fig. 9. Seasonal variations of GAI, LCC and CCC estimations on four selected IoTA systems, including AC-2 from Muizon, 41_1 DS from Boigneville, Fourques-1 from Nimes, FS-3 from Gréoux, C-B3 from Chalons and SI-3 FS52 from St-Hilaire. Red circles represent ground measurements. The measurements of IoTA didn't cover the whole growth circle as shown in Table S1.

5 Discussion

5.1 Estimation of diffuse fraction in each spectral band

Near-surface sensor measurements are affected by varying illumination conditions in natural environments. Indeed, the targeted surface receives the combination of both the direct and diffuse components of the solar irradiance, which impacts the signal measured by the sensor (Schaepman-Strub et al., 2006). Diffuse solar irradiance has important impacts on canopy photosynthesis in the context of global change (Durand et al., 2021). Accurate assessment of diffuse irradiance or diffuse fraction is essential for simulating its contribution to canopy. Previous studies have demonstrated that diffuse irradiance in each spectral band is different because the main contributors driving the proportion of diffuse radiation (e.g., clouds and aerosol) are wavelength-dependent (Kirchstetter et al., 2004). And the spectral diffuse fraction is also required by canopy radiative transfer models, such as PROSAIL. It is therefore mandatory to evaluate the diffuse fraction of irradiance during the acquisition.

The most accurate method to measure spectral diffuse irradiance is to measure normal direct irradiance and global irradiance, and then calculate diffuse irradiance or diffuse fraction from the measurements (López et al., 2004). The global irradiance is widely measured, yet the pyrheliometer instrument to measure direct normal irradiance is very expensive. Many researchers thus used alternate methods, such as pyranometer with a shadowband, or a rotating shadowband and a tracking solar disk, to measure spectral diffuse irradiance by

682 blocking direct irradiance from total irradiance (de Simón-Martín et al., 2015; Harrison et al.,
683 1999; Michalsky and Kiedron, 2022). Although the feasibility of these instruments or models
684 have been greatly improved, their cost and use do not correspond to the constraints of the
685 IoTA systems (affordable and installed without requiring RS expertise) and thus not
686 applicable in this study.

687 Alternatively, Spitters et al. (1986) indicated that the diffuse fraction in each spectral
688 band can be approximated from the PAR diffuse fraction. However, although the total PAR is
689 widely monitored in meteorological ground stations, diffuse PAR is not routinely measured.
690 Diffuse PAR is usually obtained through various semi-empirical relationships, either with the
691 diffuse fraction of the global incoming radiation (Ezhova et al., 2018; Gu et al., 2002; Spitters
692 et al., 1986), or with the ratio of total PAR to extraterrestrial PAR (Hassika and Berbigier,
693 1998; Jacovides et al., 2010, 2007). Nevertheless, the calibration of these semi-empirical
694 functions are site dependent and show poor extrapolation capacities (Gueymard and Ruiz-
695 Arias, 2016; Jacovides et al., 2007; Spitters et al., 1986; Yang and Gueymard, 2020). In this
696 study, we propose to use a fully empirical, data driven approach that does not require a priori
697 knowledge of the relationship as it consists in training some machine learning algorithm (e.g.,
698 neural networks). We trained it over a limited number of sites in this study, but its
699 applicability could be extended by adding ancillary data as inputs (meteorology, site location),
700 and collecting and gathering data under different illumination conditions and locations to
701 improve the representativeness and robustness of this method.

702 Thanks to atmospheric radiative transfer model, e.g., 6S simulations, we showed that the
703 spectral diffuse fraction present polynomial relationships with PAR diffuse fraction through
704 6S model simulations for a variety of low to high visibility conditions (Fig. 6). They are in
705 line with those reported in Spitters et al. (1986), who showed that PAR diffuse fraction can be
706 almost twice as great as that in the red part since the degree of aerosol scattering decreases as
707 the wavelength increases. This method was evaluated by setting up a simple experiment using
708 a multispectral camera. The spectral diffuse fraction in the validation experiments was
709 approximated by the ratio of the total radiance over small shaded and illuminated areas of the
710 grey carpet. Results might be affected by the distance between two measurements (around
711 500 m), a small dyssynchronization between the acquisition systems, or differences in
712 integration time, since the illumination conditions were highly variable. Note also, that
713 although the two areas were close and the radiance was extracted from the same image, the
714 grey carpet is not perfectly homogeneous and flat as compared to a spectralon, which also
715 might impact the results (Eq. S1). Promising results were obtained (Fig. 6c, Table 3) even if

some scattering occurs especially in the blue and green bands that are the most affected by aerosols. Nevertheless, these two bands do not correspond to IoTA specifications. Further experiments specifically designed for such objective should be conducted, similarly to the one developed by Michalsky and Kiedron (2022) for example. Another uncertainty might result from the 6S atmospheric correction model which does not incorporate the cloud component. To solve this, we isolated fully cloudy conditions and other conditions by setting a threshold on PAR diffuse fraction, i.e., > 0.9 represents cloudy conditions. Spectral diffuse fraction equals to PAR diffuse fraction under cloudy conditions, otherwise, they were simulated by setting large range of visibility in 6S model. More evaluations are necessary to study this isolation in multiple locations and illumination conditions.

5.2 Relative values of spectrometer measurements as inputs to inversion

This study takes advantage of previous approaches applied to satellite observation to develop an original close-range sensing method by exploiting the angular and spectral variations of the signal for GAI, LCC and CCC retrieval through kernel-driven model and PROSAIL radiative transfer model (Weiss and Baret, 1999). Due to the difficulties of absolute radiometric calibration of continuous multi-band spectrometer measurements from near-surface systems under varying illumination conditions, we used an algorithm that relies on relative values. Raw measurements from multi-band spectrometers were converted into irradiance and used to calculate the relative values. The relative values present seasonal variation of wheat during the whole growth stage and diurnal variations under different illumination conditions (Fig. S4 and Fig. S5 in Supplementary Materials Part D). Accordingly, the kernel-driven and PROSAIL model simulations were also converted into relative values to keep the consistency between simulations and measurements. Relative values were already applied to images acquired by multispectral cameras on board UAV (Jay et al., 2019; Verger et al., 2014). However, in those studies, it was designed to remove possible effects of the spatial variability of the incoming light (especially in case of clouds passing during the flight) between the reference panel used for the calibration and the image acquired by the UAV. We applied here the same principle and extended it successfully for the first time to continuous spectrometer measurements without any calibration reference measurements. The relative values can be calculated in different ways, using average of all bands as denominator (Verger et al., 2014) or using one single band as denominator (Jay et al., 2019). Our results showed that the former present overall better performance when comparing with ground measurements for GAI, LCC and CCC. This might be because the average values neutralize

749 the uncertainties among bands and thus improve the inversion accuracy. This could be further
750 checked by setting up experiments based on calibrated reflectance measurements under
751 different illumination conditions.

752 Conversely to traditional ground measurements methods based on the gap fraction theory,
753 we were able to exploit both the spectral and the angular variations of the signal with the sun
754 positions thanks to continuous acquisitions during the day. These multi-spectral and multi-
755 angle measurements are an efficient way to constrain the ill-posed inversion problem (Baret
756 and Buis, 2008) and improve the retrieval accuracy of GAI, LCC and CCC as already
757 demonstrated in UAV or satellite experiment contexts (Deng et al., 2006; Dorigo, 2012; Duan
758 et al., 2014; Roosjen et al., 2018; Roujean and Lacaze, 2002). Dorigo (2012), Duan et al.
759 (2014) and Roosjen et al. (2018) applied Look-up tables in the inversion, while Deng et al.
760 (2006) and Roujean and Lacaze (2002) normalized multi-angle reflectance into specific view
761 angles using kernel-driven models and estimated biophysical variable using normalized
762 values. However, simple application of above methods is not feasible in the continuous
763 spectrometer measurements. In this study, some invalid measurements (e.g., sun zenith angle
764 larger than 60° or negative measurements) were removed before the inversion and the sun
765 position vary every day, resulting in different number of valid measurements and
766 corresponding geometry per day. This will increase the dimension of training database for
767 look-up table and impact the efficiency in the inversion. Alternatively, we combined the
768 kernel-driven model and PROSAIL model and estimated biophysical variables from an BP-
769 ANN algorithm. BP-ANN inversion technique has proven to be successful on an operational
770 basis thanks to its accuracy and efficiency (Verrelst et al., 2015). A fixed number of inputs is
771 required to use BP-ANN. Nevertheless, the number of valid measurements from multi-band
772 spectrometer during a day varies, putting obstacles on the use of BP-ANN. A kernel-driven
773 model (Roujean et al., 1992) was thus introduced to reduce the dimension in training and
774 inversion. Kernel parameters of each band were calculated from diurnal measurements,
775 leading to 18 kernel parameters for six bands (three per band) in total. These kernel
776 parameters were used as inputs of BP-ANN to invert daily GAI, LCC and CCC. The quite
777 good estimation accuracy of canopy biophysical variables reveals the feasibility of this
778 method.

779 At least 18 measurements are required to compute daily BRDF kernel parameters (6
780 bands × 3 kernels) using optimization algorithms. In fact, more than 90% of days satisfy this
781 requirement because the IoTA measurements were taken every 15 minutes. However, the GAI
782 estimation using data from one day measurement may present some shaky profiles as shown

in Fig. 10. A moving-window strategy was therefore applied, thus filling gaps and minimizing the impact of outliers on the inversion process. After investigating the optimal window size, we decided to use 3 days moving window to capture the rapid changes of crops while keeping good accuracy of kernel parameter estimation. This is in agreement with Hufkens et al. (2019) who kept the sites that have up to 2.9 images per week during the peak of growing seasonal. As a matter for fact, in the fast growing stages (e.g., tillering and stem extension) and ripening stages (Magney et al., 2016), the assumption that wheat status is stable in 3 days remains reasonable but not acceptable for 5 or 7 days. Even during the heading period when the wheat NDVI changes slowly, Velumani et al. (2020) found that there are around 3 days from the emergence of the spikes from the stem to the end of heading.

5.3 Accuracy of daily GAI, LCC and CCC estimations

The good accuracy of GAI, LCC and CCC demonstrated the feasibility of this method despite the absence of absolute radiometric calibration of the multi-band spectrometer. GAI was well estimated with acceptable RMSE and relative RMSE, consistent with previous studies using close-range monitoring systems (Chen et al., 2022; Kim et al., 2019; Rogers et al., 2021). For leaf chlorophyll content of wheat, similar results by PROSAIL inversion based on close-range measurements were also reported in other studies. The RMSE obtained in this study (15.49 µg/cm^2) is lower than that reported by Botha et al. (2010) (15.61 – 23.31 µg/cm^2) that was estimated by hyperspectral reflectance over wheat canopy in different stages. Using a field goniometer multi-angle hyperspectral reflectance, Lunagaria and Patel (2019) obtained a RMSE of 15.62 µg/cm^2 over wheat based on all angles and reached a lower RMSE of 10.5 µg/cm^2 when reducing the angular sampling around the hotspot direction. Other studies have shown better performances on LCC estimation by calibrating relationships with vegetation indices, like for example Li et al., (2022) (RMSE of 6.22 – 6.87 µg/cm^2) using soil-removed semi-empirical model or Jay et al. (2019) (RMSE less than 5 µg/cm^2) who computed vegetation indices only on pixels corresponding to vegetation elements from hyperspectral images acquired by a drone. However, these empirical relationships may not be transferable to other contexts (wheat cultivars, soil background, acquisition conditions). The systematic bias of IoTA LCC is mainly resulted from the reference LCC which is discussed below. Note that CCC is less affected by calibration as it is an integrated value at the canopy level. Our results are similar to Jay et al. (2017b) who also obtained better results of CCC estimation (R^2 = 0.76) than LCC (R^2 = 0.26) over sugarbeet from both radiative transfer models inversion and empirical relationships with vegetation indices. Conversely to

vegetation indices, our method does not require absolute calibration of the signal or ground measurements to fit an empirical relationship.

Although the overall accuracy of GAI, LCC and CCC is acceptable and comparable with previous studies, uncertainties still exist and influence the validation results. GAI was retrieved from the inversion of the PROSAIL 1-D radiative transfer model (Jacquemoud et al., 2009; Verrelst et al., 2019; Weiss et al., 2002), which does not consider either the vegetation clumping or row effect at early wheat stages. Therefore, the proposed approach allows to assess the effective value GAI (Yan et al., 2019), which is consistent with our reference effective GAI calculated from RGB gap fraction. Indeed, Jiang et al., (2022) showed that for wheat and maize, effective GAI is better estimated from reflectance measurements as compared to the true GAI even when considering the clumping effect through the use of a 3D radiative transfer model. They also showed that, even with a 1D-RTM model inversion, effective GAI is better estimated than effective LAI for non-reproductive stages, which was the case of this study. Note also that effective GAI is better suited than true LAI to describe the light interception within the canopy, which is a key component of crop growth models. Considering LCC, calibration issues may impact the actual location of the inflection point in the red-edge domain which is very sensitive to LCC content (Gitelson et al., 1996). More efforts are required in the future to deeply study the influences of radiometric calibration on LCC estimations using data at canopy level. The early version PROSPECT model (Jacquemoud and Baret, 1990) was used in this study, while several improved PROSPECT models were proposed, such as PROSPECT-D (Féret et al., 2017) and FASPECT (Jiang et al., 2021) which have been proved to have better LCC retrieval accuracy (Berger et al., 2018; Jiang et al., 2021; Li et al., 2020). Further, the range of input parameters for generating the training database also has direct impacts on the retrieval accuracy. For example, chlorophyll a+b content for wheat varies within 0 - 90 ug/cm^2, e.g., 10 - 80 ug/cm^2 in Li et al., (2022), 0 - 80 ug/cm^2 in Berger et al., (2018) and 20 - 90 ug/cm^2 in Delloye et al., (2018). We finally set the range to 20-80 ug/cm^2 based on prior knowledge of the wheat in our study area. The ALA of wheat was demonstrated to be erectophile (from 70° to 80°), therefore, the ALA for PROSAIL model was set to 60° – 80° with mean of 70°. This is consistent with Dong et al., (2019) which characterized wheat by erectophile leaf angle distribution with mean ALA of 62.49° and standard deviation of 11.08°.

The accuracy of estimated GAI, LCC and CCC relies on the ground reference dataset. In this study, reference GAI was estimated from gap fraction based on segmentation of green pixels on RGB images. We used a robust deep learning method trained on a comprehensive

dataset composed of a variety of species, instruments, and environmental conditions (Madec et al., 2023; Serouart et al., 2022) to guarantee the accuracy of segmentation. It is worth noting the segmentation might be difficult when GAI is larger than 4 or 5. The derivation of the GAI reference dataset assumes a constant G-function for a 45° viewing direction. This is actually very similar to the approach validated by Campos-Taberner et al., (2016) and Francone et al., (2014), who used the 57.5° angle for which the G-function is constant regardless of the leaf inclination angle value. We preferred using a 45° which show less saturation for dense canopies and eases the RGB image segmentation. At 45°, G can still be assumed constant for wheat canopies that were shown erectophile (mean inclination angle between 70° and 74° as estimated by Barillot et al., (2019) for different wheat types). Additionally, this allows to be consistent with the inclination angle of the multi-band spectrometer. When using a single camera, the choice of the viewing angle to get a constant G-function over other crop types need further investigations. This can be overcome by using at least two cameras looking in different view angles to concurrently assess GAI and inclination angle (Weiss et al., 2004).

SPAD meters are routinely used to measure chlorophyll content in the field. Calibration of raw SPAD readings to LCC is a critical step before using them in validation. The strictest calibration procedure is composed of three steps: cutting several leaves samples in regular shapes and recording multiple SPAD readings per sample, measuring absolute LCC of these samples in laboratory through standard wet chemistry procedures (Lichtenthaler and Wellburn, 1983), and establishing empirical relationships between the absolute LCC and SPAD values for each variety of wheat. However, this procedure is time-consuming and impractical for large number of samples. One alternative solution is to apply existing equations from literatures to our SPAD readings to obtain the LCC values. Previous studies showed that the calibration equations are various in the format (linear, polynomial, exponential or homographic)(Cerovic et al., 2012; Zhang et al., 2022). For a single format, the coefficients are also different depending on the species and measurement periods, although the differences of might be very small as reported by Uddling et al., (2007) and Zhang et al., (2022). Since there was no absolute reference LCC in this study, choosing which calibration equation has direct impacts on the validation results. Applying available twelve equations built for wheat or with wheat, we found a very similar correlation between IoTA LCC and reference LCC (R^2 between 0.51 and 0.53, Fig. S8) with some bias depending on relationship (RMSE between 5.59 µg/cm^2 – 18.94 µg/cm^2, Fig. S8), which actually questions the reliability of the SPAD to actually assess the LCC without any specific calibration. A generic

approach for this calibration remains lack. To solve this, we proposed an ensemble method to compute the median of LCC converted from all available equations as the reference, which could evaluate IoTA LCC to some extent. Nevertheless, the reference itself has an overall uncertainty of 7.44 µg/cm^2, and it greatly relies on selected calibration equations. Further studies are urgently required to investigate a reliable and generic calibration method to convert SPAD readings into absolute LCC. Furthermore, this uncertainty may be also related to the SPAD sampling protocol. We measured only the top leaves as suggested by many other research teams (De Grave et al., 2021; Zhou et al., 2020) while the vertical chlorophyll distribution within the wheat canopy may have some influence, also depending on the phenological stage. Indeed, few studies investigated this aspect and we found contradictory results about this distribution with higher chlorophyll content measured at the upper layer (T. Wang et al., 2022; Wu et al., 2021) using destructive measurements, while Li et al., (2019) found that the highest chlorophyll content in the middle of the canopy (SPAD). Besides the measurement method, more investigations are needed regarding the sampling protocol.

Regarding the canopy chlorophyll content, we assumed it constant during a three-day period which corresponds to the size of the moving window selected for our algorithm. Additionally, the PROSAIL model assumes a turbid medium only composed of leaves, therefore CCC was computed as the product of the leaf chlorophyll content by effective LAI. This is consistent with the SPAD reference measurements acquired over top leaves during our measurement period that does not include reproductive stage (e.g., presence of ears). Indeed, from the top of canopy, the signal captured from the multi-band spectrometers comes mainly from the leaves, reducing the possible impact of differences in chlorophyll content between stems and leaves. However, the chlorophyll content and its contribution to CCC and canopy reflectance of other elements than green leaves (e.g., stems, ears, mix of green and yellow leaves between the senescent phase) should be better investigated following the studies of Li et al., (2021) who showed experimentally a significant impact of ears on the measured NDVI (around 9%), and Jiang et al., (2022) who used a 3D radiative transfer model to evaluate the impact of yellow stems and leaves on the reflectance signal or Amin et al., (2021) who trained a machine learning algorithm to estimate Green and Brown GAI from Sentinel-2 using experimental data.

5.4 Limitations and implications

Constrained by the low-cost instrument design, this algorithm uses several approximations that may impact the retrieval accuracy. Although we made some attempts to evaluate each step, further investigations are needed to strengthen these results: (i) additional measurements should be used to allow good generalization capacities of PAR diffuse fraction estimation. This could be achieved by making use of site networks such as FLUXNET (ii) the relationships between the diffuse fraction in the PAR and in other wavebands derived from the 6S model should be better investigated by setting up a proper experiment (iii) the uncertainties associated to the use of relative reflectance should be better investigated by comparing with an approach based on absolute and calibrated reflectance using experimental setups like the one developed by Michalsky and Kiedron (2022) (iv) completing the validation campaign with more reference points and simultaneous LCC laboratory and SPAD measurements to strengthen the SPAD/LCC relationships.

Based on this common feature, we developed a practical and computationally efficient approach that allows inverting a radiative transfer model in situations where measuring incoming radiance is not feasible, and/or acquisitions are acquired with a variable geometry by normalizing the data (e.g., relative radiance value, use of kernel BRDF models). This could be particularly useful when using UAV data during unstable cloud conditions or monitoring closed canopies where installing sensors to measure incoming might not be feasible. We also proposed a simple mean to characterize the incoming diffuse fraction from incident PAR measurements, although the relationship to estimate diffuse PAR from incoming radiation should be strengthen by using additional meteorological measurements. Deploying networks of IoTA systems would allow to better assess the within and between fields heterogeneity and provide valuable information to decision support systems and farmers.

6 Conclusions

Non-destructive measurements of daily GAI, LCC and CCC offer insightful information to monitor crop status. Whilst substantial efforts have been devoted to monitor continuous GAI through near-surface platforms, concurrent and autonomous monitoring GAI, LCC and CCC is scarce. In this study, we developed a comprehensive approach to estimate canopy GAI, LCC and CCC from a near-surface monitoring system with a low-cost multi-band spectrometer multispectral spectrometers and a PAR. This approach overcomes several

challenges related to the use of multi-band spectrometer from near-surface system in natural environment, through estimation of various diffuse fraction in each spectral band and consideration of multi-angle observations. We validated the accuracy of this approach using 43 IoTA systems in wheat fields. Our results indicate that this algorithm works well for the multi-band spectrometer installed on the near-surface platforms, to track wheat GAI, CCC, and in a lesser extent LCC simultaneously at a daily temporal resolution. We demonstrated that multi-angle information can be properly used to retrieve variables using ANN inversion strategy, based on the combined use of kernel-driven BRDF and PROSAIL models. In addition, we provide a practical method to derive the spectral diffuse fraction from PAR sensor measurements, based on empirical relationships for PAR diffuse/direct partitioning and model simulations to relate spectral to PAR diffuse fractions. Compared with reference data, our method achieved satisfactory performances with GAI (RMSE = 0.51), LCC (RMSE = 8.44 µg/cm^2), CCC (RMSE = 0.25 g/m^2) and. Given the advantages of this algorithm and comparable low cost of multi-band spectrometers and PAR sensors, we recommend it to be applied over other crops or other near-surface platforms for simultaneous estimations of GAI, LCC and CCC. More measurements on multiple crops and under different climate conditions are needed to further investigate the robustness of the algorithm. For next generations of such IoT observation system, sensors able to measure spectral and diffuse irradiance directly such as those developed for the purpose of observing solar-induced fluorescence should be evaluated (e.g., the accuracy, price and possibility for large deployment in a field). Furthermore, as demonstrated by numerous previous studies, adding sensors with a band located in the green domain could be added to improve GAI, LCC and CCC inversion (Daughtry, 2000; Gitelson et al., 2003; Weiss et al., 2000). More efforts will also be put to explore the combination of RGB camera and the multi-band spectrometer to retrieve GAI, LCC and CCC.

7 Acknowledgements

This work was supported by French FUI IOTA project (FUI 24 – D0S0071619). The authors acknowledge Guy Deshayes and Simon Madec (Arvalis) for their kind supports with reference data collection and processing and Jeremy Labrosse (HIPHEN) for his valuable supports on IoTA systems' maintenance. Wenjuan Li acknowledges support from Central Public-interest Scientific Institution Basal Research Fund (No. CAAS-ZDRW202107) and National Natural Science Foundation of China (42201388). The authors are thankful to the

anonymous reviewers for their constructive criticism which contributed to improve substantially the paper.

8 References

Amin, E., Verrelst, J., Rivera-Caicedo, J.P., Pipia, L., Ruiz-Verdú, A., Moreno, J., 2021. Prototyping Sentinel-2 green LAI and brown LAI products for cropland monitoring. Remote Sensing of Environment 255, 112168. https://doi.org/10.1016/j.rse.2020.112168

Baresel, J.P., Rischbeck, P., Hu, Y., Kipp, S., Hu, Y., Barmeier, G., Mistele, B., Schmidhalter, U., 2017. Use of a digital camera as alternative method for non-destructive detection of the leaf chlorophyll content and the nitrogen nutrition status in wheat. Computers and Electronics in Agriculture 140, 25–33. https://doi.org/10.1016/j.compag.2017.05.032

Baret, F., Buis, S., 2008. Estimating Canopy Characteristics from Remote Sensing Observations: Review of Methods and Associated Problems, in: Liang, S. (Ed.), Advances in Land Remote Sensing. Springer Netherlands, Dordrecht, pp. 173–201. https://doi.org/10.1007/978-1-4020-6450-0_7

Baret, F., de Solan, B., Lopez-Lozano, R., Ma, K., Weiss, M., 2010. GAI estimates of row crops from downward looking digital photos taken perpendicular to rows at 57.5° zenith angle: Theoretical considerations based on 3D architecture models and application to wheat crops. Agricultural and Forest Meteorology 150, 1393–1401. https://doi.org/10.1016/j.agrformet.2010.04.011

Barillot, R., Chambon, C., Fournier, C., Combes, D., Pradal, C., Andrieu, B., 2019. Investigation of complex canopies with a functional–structural plant model as exemplified by leaf inclination effect on the functioning of pure and mixed stands of wheat during grain filling. Annals of Botany 123, 727–742. https://doi.org/10.1093/aob/mcy208

Berger, K., Atzberger, C., Danner, M., D'Urso, G., Mauser, W., Vuolo, F., Hank, T., 2018. Evaluation of the PROSAIL Model Capabilities for Future Hyperspectral Model Environments: A Review Study. Remote Sensing 10, 85. https://doi.org/10.3390/rs10010085

Berger, K., Verrelst, J., Féret, J.-B., Wang, Z., Wocher, M., Strathmann, M., Danner, M., Mauser, W., Hank, T., 2020. Crop nitrogen monitoring: Recent progress and principal developments in the context of imaging spectroscopy missions. Remote Sensing of Environment 242, 111758. https://doi.org/10.1016/j.rse.2020.111758

Botha, E.J., Leblon, B., Zebarth, B.J., Watmough, J., 2010. Non-destructive estimation of wheat leaf chlorophyll content from hyperspectral measurements through analytical model inversion. International Journal of Remote Sensing 31, 1679–1697. https://doi.org/10.1080/01431160902926574

Campbell, P., Huemmrich, K., Middleton, E., Ward, L., Julitta, T., Daughtry, C., Burkart, A., Russ, A., Kustas, W., 2019. Diurnal and Seasonal Variations in Chlorophyll Fluorescence

Associated with Photosynthesis at Leaf and Canopy Scales. Remote Sensing 11, 488. https://doi.org/10.3390/rs11050488

Campos-Taberner, M., García-Haro, F., Confalonieri, R., Martínez, B., Moreno, Á., Sánchez-Ruiz, S., Gilabert, M., Camacho, F., Boschetti, M., Busetto, L., 2016. Multitemporal Monitoring of Plant Area Index in the Valencia Rice District with PocketLAI. Remote Sensing 8, 202. https://doi.org/10.3390/rs8030202

Cao, S., Danielson, B., Clare, S., Koenig, S., Campos-Vargas, C., Sanchez-Azofeifa, A., 2019. Radiometric calibration assessments for UAS-borne multispectral cameras: Laboratory and field protocols. ISPRS Journal of Photogrammetry and Remote Sensing 149, 132–145. https://doi.org/10.1016/j.isprsjprs.2019.01.016

Cerovic, Z.G., Masdoumier, G., Ghozlen, N.B., Latouche, G., 2012. A new optical leaf- clip meter for simultaneous non- destructive assessment of leaf chlorophyll and epidermal flavonoids. Physiologia Plantarum 146, 251–260. https://doi.org/10.1111/j.1399-3054.2012.01639.x

Chen, J.M., Black, T.A., 1992. Defining leaf area index for non-flat leaves. Plant Cell Environ 15, 421–429. https://doi.org/10.1111/j.1365-3040.1992.tb00992.x

Chen, Y., Jiao, S., Cheng, Y., Wei, H., Sun, L., Sun, Y., 2022. LAI-NOS: An automatic network observation system for leaf area index based on hemispherical photography. Agricultural and Forest Meteorology 322, 108999. https://doi.org/10.1016/j.agrformet.2022.108999

Chianucci, F., Bajocco, S., Ferrara, C., 2021. Continuous observations of forest canopy structure using low-cost digital camera traps. Agricultural and Forest Meteorology 307, 108516. https://doi.org/10.1016/j.agrformet.2021.108516

Cogliati, S., Rossini, M., Julitta, T., Meroni, M., Schickling, A., Burkart, A., Pinto, F., Rascher, U., Colombo, R., 2015a. Continuous and long-term measurements of reflectance and sun-induced chlorophyll fluorescence by using novel automated field spectroscopy systems. Remote Sensing of Environment 164, 270–281. https://doi.org/10.1016/j.rse.2015.03.027

Cogliati, S., Rossini, M., Julitta, T., Meroni, M., Schickling, A., Burkart, A., Pinto, F., Rascher, U., Colombo, R., 2015b. Continuous and long-term measurements of reflectance and sun-induced chlorophyll fluorescence by using novel automated field spectroscopy systems. Remote Sensing of Environment 164, 270–281. https://doi.org/10.1016/j.rse.2015.03.027

Croft, H., Chen, J.M., Luo, X., Bartlett, P., Chen, B., Staebler, R.M., 2017. Leaf chlorophyll content as a proxy for leaf photosynthetic capacity. Glob Change Biol 23, 3513–3524. https://doi.org/10.1111/gcb.13599

Darvishzadeh, R., Matkan, A.A., Dashti Ahangar, A., 2012. Inversion of a Radiative Transfer Model for Estimation of Rice Canopy Chlorophyll Content Using a Lookup-Table Approach. IEEE J. Sel. Top. Appl. Earth Observations Remote Sensing 5, 1222–1230. https://doi.org/10.1109/JSTARS.2012.2186118

Daughtry, C., 2000. Estimating Corn Leaf Chlorophyll Concentration from Leaf and Canopy Reflectance. Remote Sensing of Environment 74, 229–239. https://doi.org/10.1016/S0034-4257(00)00113-9

De Grave, C., Pipia, L., Siegmann, B., Morcillo-Pallarés, P., Rivera-Caicedo, J.P., Moreno, J., Verrelst, J., 2021. Retrieving and Validating Leaf and Canopy Chlorophyll Content at Moderate Resolution: A Multiscale Analysis with the Sentinel-3 OLCI Sensor. Remote Sensing 13, 1419. https://doi.org/10.3390/rs13081419

de Simón-Martín, M., Alonso-Tristán, C., González-Peña, D., Díez-Mediavilla, M., 2015. New device for the simultaneous measurement of diffuse solar irradiance on several azimuth and tilting angles. Solar Energy 119, 370–382. https://doi.org/10.1016/j.solener.2015.06.001

Delloye, C., Weiss, M., Defourny, P., 2018. Retrieval of the canopy chlorophyll content from Sentinel-2 spectral bands to estimate nitrogen uptake in intensive winter wheat cropping systems. Remote Sensing of Environment 216, 245–261. https://doi.org/10.1016/j.rse.2018.06.037

Delta-T Devices Ltd, 2002. User Manual for the Sunshine Sensor type BF3.

Deng, F., Chen, J.M., Plummer, S., Mingzhen Chen, Pisek, J., 2006. Algorithm for global leaf area index retrieval using satellite imagery. IEEE Trans. Geosci. Remote Sensing 44, 2219–2229. https://doi.org/10.1109/TGRS.2006.872100

do Amaral, E.S., Vieira Silva, D., Dos Anjos, L., Schilling, A.C., Dalmolin, Â.C., Mielke, M.S., 2019. Relationships between reflectance and absorbance chlorophyll indices with RGB (Red, Green, Blue) image components in seedlings of tropical tree species at nursery stage. New Forests 50, 377–388. https://doi.org/10.1007/s11056-018-9662-4

Dong, T., Liu, J., Shang, J., Qian, B., Ma, B., Kovacs, J.M., Walters, D., Jiao, X., Geng, X., Shi, Y., 2019. Assessment of red-edge vegetation indices for crop leaf area index estimation. Remote Sensing of Environment 222, 133–143. https://doi.org/10.1016/j.rse.2018.12.032

Dong, Y., Jiao, Z., Ding, A., Zhang, H., Zhang, X., Li, Y., He, D., Yin, S., Cui, L., 2018. A modified version of the kernel-driven model for correcting the diffuse light of ground multi-angular measurements. Remote Sensing of Environment 210, 325–344. https://doi.org/10.1016/j.rse.2018.03.030

Dorigo, W.A., 2012. Improving the Robustness of Cotton Status Characterisation by Radiative Transfer Model Inversion of Multi-Angular CHRIS/PROBA Data. IEEE J. Sel. Top. Appl. Earth Observations Remote Sensing 5, 18–29. https://doi.org/10.1109/JSTARS.2011.2171181

Duan, S.-B., Li, Z.-L., Wu, H., Tang, B.-H., Ma, L., Zhao, E., Li, C., 2014. Inversion of the PROSAIL model to estimate leaf area index of maize, potato, and sunflower fields from unmanned aerial vehicle hyperspectral data. International Journal of Applied Earth Observation and Geoinformation 26, 12–20. https://doi.org/10.1016/j.jag.2013.05.007

Durand, M., Murchie, E.H., Lindfors, A.V., Urban, O., Aphalo, P.J., Robson, T.M., 2021. Diffuse solar radiation and canopy photosynthesis in a changing environment. Agricultural and Forest Meteorology 311, 108684. https://doi.org/10.1016/j.agrformet.2021.108684

Ezhova, E., Ylivinkka, I., Kuusk, J., Komsaare, K., Vana, M., Krasnova, A., Noe, S., Arshinov, M., Belan, B., Park, S.-B., Lavrič, J.V., Heimann, M., Petäjä, T., Vesala, T., Mammarella, I., Kolari, P., Bäck, J., Rannik, Ü., Kerminen, V.-M., Kulmala, M., 2018. Direct effect of aerosols on solar radiation and gross primary production in boreal and hemiboreal forests. Atmos. Chem. Phys. 18, 17863–17881. https://doi.org/10.5194/acp-18-17863-2018

Fang, H., Baret, F., Plummer, S., Schaepman- Strub, G., 2019. An Overview of Global Leaf Area Index (LAI): Methods, Products, Validation, and Applications. Rev. Geophys. 57, 739–799. https://doi.org/10.1029/2018RG000608

Fang, H., Ye, Y., Liu, W., Wei, S., Ma, L., 2018. Continuous estimation of canopy leaf area index (LAI) and clumping index over broadleaf crop fields: An investigation of the PASTIS-57 instrument and smartphone applications. Agricultural and Forest Meteorology 253–254, 48–61. https://doi.org/10.1016/j.agrformet.2018.02.003

FAO (Ed.), 2017. The future of food and agriculture: trends and challenges. Food and Agriculture Organization of the United Nations, Rome.

Féret, J.-B., Gitelson, A.A., Noble, S.D., Jacquemoud, S., 2017. PROSPECT-D: Towards modeling leaf optical properties through a complete lifecycle. Remote Sensing of Environment 193, 204–215. https://doi.org/10.1016/j.rse.2017.03.004

Fletcher, R.S., Fisher, D.K., 2018. A Miniature Sensor for Measuring Reflectance, Relative Humidity, and Temperature: A Greenhouse Example. AS 09, 1516–1527. https://doi.org/10.4236/as.2018.911106

Francone, C., Pagani, V., Foi, M., Cappelli, G., Confalonieri, R., 2014. Comparison of leaf area index estimates by ceptometer and PocketLAI smart app in canopies with different structures. Field Crops Research 155, 38–41. https://doi.org/10.1016/j.fcr.2013.09.024

Garrity, S.R., Vierling, L.A., Bickford, K., 2010. A simple filtered photodiode instrument for continuous measurement of narrowband NDVI and PRI over vegetated canopies. Agricultural and Forest Meteorology 150, 489–496. https://doi.org/10.1016/j.agrformet.2010.01.004

GCOS, 2011. Systematic observation requirements for satellite- based products for climate, 2011 Update, Supplemental Details to the Satellite- Based Component of the Implementation Plan for the Global Observing System for Climate in Support of the UNFCCC (2010 Update).

Gitelson, A.A., 2005. Remote estimation of canopy chlorophyll content in crops. Geophys. Res. Lett. 32, L08403. https://doi.org/10.1029/2005GL022688

Gitelson, A.A., Gritz †, Y., Merzlyak, M.N., 2003. Relationships between leaf chlorophyll content and spectral reflectance and algorithms for non-destructive chlorophyll assessment in higher plant leaves. Journal of Plant Physiology 160, 271–282. https://doi.org/10.1078/0176-1617-00887

Gitelson, A.A., Merzlyak, M.N., Lichtenthaler, H.K., 1996. Detection of Red Edge Position and Chlorophyll Content by Reflectance Measurements Near 700 nm. Journal of Plant Physiology 148, 501–508. https://doi.org/10.1016/S0176-1617(96)80285-9

Gitelson, A.A., Peng, Y., Huemmrich, K.F., 2014. Relationship between fraction of radiation absorbed by photosynthesizing maize and soybean canopies and NDVI from remotely sensed data taken at close range and from MODIS 250m resolution data. Remote Sensing of Environment 147, 108–120. https://doi.org/10.1016/j.rse.2014.02.014

Grossmann, K., Frankenberg, C., Magney, T.S., Hurlock, S.C., Seibt, U., Stutz, J., 2018a. PhotoSpec: A new instrument to measure spatially distributed red and far-red Solar-Induced Chlorophyll Fluorescence. Remote Sensing of Environment 216, 311–327. https://doi.org/10.1016/j.rse.2018.07.002

Grossmann, K., Frankenberg, C., Magney, T.S., Hurlock, S.C., Seibt, U., Stutz, J., 2018b. PhotoSpec: A new instrument to measure spatially distributed red and far-red Solar-Induced Chlorophyll Fluorescence. Remote Sensing of Environment 216, 311–327. https://doi.org/10.1016/j.rse.2018.07.002

Gu, L., Baldocchi, D., Verma, S.B., Black, T.A., Vesala, T., Falge, E.M., Dowty, P.R., 2002. Advantages of diffuse radiation for terrestrial ecosystem productivity: ADVANTAGES OF DIFFUSE RADIATION. J. Geophys. Res. 107, ACL 2-1-ACL 2-23. https://doi.org/10.1029/2001JD001242

Gueymard, C.A., Ruiz-Arias, J.A., 2016. Extensive worldwide validation and climate sensitivity analysis of direct irradiance predictions from 1-min global irradiance. Solar Energy 128, 1–30. https://doi.org/10.1016/j.solener.2015.10.010

Guo, Y., Yin, G., Sun, H., Wang, H., Chen, S., Senthilnath, J., Wang, J., Fu, Y., 2020. Scaling Effects on Chlorophyll Content Estimations with RGB Camera Mounted on a UAV Platform Using Machine-Learning Methods. Sensors 20, 5130. https://doi.org/10.3390/s20185130

Harrison, L., Beauharnois, M., Berndt, J., Kiedron, P., Michalsky, J., Min, Q., 1999. The rotating shadowband spectroradiometer (RSS) at SGP. Geophys. Res. Lett. 26, 1715–1718. https://doi.org/10.1029/1999GL900328

Hassika, P., Berbigier, P., 1998. Annual cycle of photosynthetically active radiation in maritime pine forest. Agricultural and Forest Meteorology 90, 157–171. https://doi.org/10.1016/S0168-1923(98)00054-9

Heusinkveld, B.G., Mol, W.B., Van Heerwaarden, C.C., 2023. A new accurate low-cost instrument for fast synchronized spatial measurements of light spectra. Atmos. Meas. Tech. 16, 3767–3785. https://doi.org/10.5194/amt-16-3767-2023

Hufkens, K., Melaas, E.K., Mann, M.L., Foster, T., Ceballos, F., Robles, M., Kramer, B., 2019. Monitoring crop phenology using a smartphone based near-surface remote sensing approach.

Agricultural and Forest Meteorology 265, 327–337. https://doi.org/10.1016/j.agrformet.2018.11.002

Jacovides, C.P., Boland, J., Asimakopoulos, D.N., Kaltsounides, N.A., 2010. Comparing diffuse radiation models with one predictor for partitioning incident PAR radiation into its diffuse component in the eastern Mediterranean basin. Renewable Energy 35, 1820–1827. https://doi.org/10.1016/j.renene.2009.11.015

Jacovides, C.P., Tymvios, F.S., Assimakopoulos, V.D., Kaltsounides, N.A., 2007. The dependence of global and diffuse PAR radiation components on sky conditions at Athens, Greece. Agricultural and Forest Meteorology 143, 277–287. https://doi.org/10.1016/j.agrformet.2007.01.004

Jacquemoud, S., Baret, F., 1990. PROSPECT: A model of leaf optical properties spectra. Remote Sensing of Environment 34, 75–91. https://doi.org/10.1016/0034-4257(90)90100-Z

Jacquemoud, S., Verhoef, W., Baret, F., Bacour, C., Zarco-Tejada, P.J., Asner, G.P., François, C., Ustin, S.L., 2009. PROSPECT+SAIL models: A review of use for vegetation characterization. Remote Sensing of Environment 113, S56–S66. https://doi.org/10.1016/j.rse.2008.01.026

Jay, S., Baret, F., Dutartre, D., Malatesta, G., Héno, S., Comar, A., Weiss, M., Maupas, F., 2019. Exploiting the centimeter resolution of UAV multispectral imagery to improve remote-sensing estimates of canopy structure and biochemistry in sugar beet crops. Remote Sensing of Environment 231, 110898. https://doi.org/10.1016/j.rse.2018.09.011

Jay, S., Maupas, F., Bendoula, R., Gorretta, N., 2017. Retrieving LAI, chlorophyll and nitrogen contents in sugar beet crops from multi-angular optical remote sensing: Comparison of vegetation indices and PROSAIL inversion for field phenotyping. Field Crops Research 210, 33–46. https://doi.org/10.1016/j.fcr.2017.05.005

Jiang, J., Comar, A., Weiss, M., Baret, F., 2021. FASPECT: A model of leaf optical properties accounting for the differences between upper and lower faces. Remote Sensing of Environment 253, 112205. https://doi.org/10.1016/j.rse.2020.112205

Jiang, J., Weiss, M., Liu, S., Baret, F., 2022. Effective GAI is best estimated from reflectance observations as compared to GAI and LAI: Demonstration for wheat and maize crops based on 3D radiative transfer simulations. Field Crops Research 283, 108538. https://doi.org/10.1016/j.fcr.2022.108538

Kim, J., Ryu, Y., Dechant, B., 2022. Development of a filter-based near-surface remote sensing system to retrieve far-red sun-induced chlorophyll fluorescence. Remote Sensing of Environment 283, 113311. https://doi.org/10.1016/j.rse.2022.113311

Kim, J., Ryu, Y., Jiang, C., Hwang, Y., 2019. Continuous observation of vegetation canopy dynamics using an integrated low-cost, near-surface remote sensing system. Agricultural and Forest Meteorology 264, 164–177. https://doi.org/10.1016/j.agrformet.2018.09.014

Kirchstetter, T.W., Novakov, T., Hobbs, P.V., 2004. Evidence that the spectral dependence of light absorption by aerosols is affected by organic carbon: SPECTRAL LIGHT ABSORPTION BY AEROSOLS. J. Geophys. Res. 109, n/a-n/a. https://doi.org/10.1029/2004JD004999

Kraft, D., 1988. A software package for sequential quadratic programming (Tech. Rep. DFVLR-FB 88-28). DLR German Aerospace Center – Institute for Flight Mechanics, Koln, Germany.

Lemaire, G., Tang, L., Bélanger, G., Zhu, Y., Jeuffroy, M.-H., 2021. Forward new paradigms for crop mineral nutrition and fertilization towards sustainable agriculture. European Journal of Agronomy 125, 126248. https://doi.org/10.1016/j.eja.2021.126248

Li, D., Chen, J.M., Yu, W., Zheng, H., Yao, X., Cao, W., Wei, D., Xiao, C., Zhu, Y., Cheng, T., 2022. Assessing a soil-removed semi-empirical model for estimating leaf chlorophyll content. Remote Sensing of Environment 282, 113284. https://doi.org/10.1016/j.rse.2022.113284

Li, D., Chen, J.M., Zhang, X., Yan, Y., Zhu, J., Zheng, H., Zhou, K., Yao, X., Tian, Y., Zhu, Y., Cheng, T., Cao, W., 2020. Improved estimation of leaf chlorophyll content of row crops from canopy reflectance spectra through minimizing canopy structural effects and optimizing off-noon observation time. Remote Sensing of Environment 248, 111985. https://doi.org/10.1016/j.rse.2020.111985

Li, W., Comar, A., Weiss, M., Jay, S., Colombeau, G., Lopez-Lozano, R., Madec, S., Baret, F., 2021a. A double swath configuration for improving throughput and accuracy of trait estimate from UAV images. Plant Phenomics 2021, 1–11. https://doi.org/10.34133/2021/9892647

Li, W., Jiang, J., Weiss, M., Madec, S., Tison, F., Philippe, B., Comar, A., Baret, F., 2021b. Impact of the reproductive organs on crop BRDF as observed from a UAV. Remote Sensing of Environment 259, 112433. https://doi.org/10.1016/j.rse.2021.112433

Li, W., Weiss, M., Waldner, F., Defourny, P., Demarez, V., Morin, D., Hagolle, O., Baret, F., 2015. A generic algorithm to estimate LAI, FAPAR and FCOVER variables from SPOT4_HRVIR and Landsat sensors: evaluation of the consistency and comparison with ground measurements. Remote Sensing 7, 15494–15516. https://doi.org/10.3390/rs71115494

Li, Y., Song, H., Zhou, L., Xu, Z., Zhou, G., 2019. Vertical distributions of chlorophyll and nitrogen and their associations with photosynthesis under drought and rewatering regimes in a maize field. Agricultural and Forest Meteorology 272–273, 40–54. https://doi.org/10.1016/j.agrformet.2019.03.026

Lichtenthaler, H.K., Wellburn, A.R., 1983. Determination of total carotenoids and chlorophylls a and b of leaf in different solvents. Biochemical Society Transactions 603, 591–592. https://doi.org/10.1016/0076-6879(87)48036-1

López, G., Muneer, T., Claywell, R., 2004. Assessment of four shadow band correction models using beam normal irradiance data from the United Kingdom and Israel. Energy Conversion and Management 45, 1963–1979. https://doi.org/10.1016/j.enconman.2003.11.001

Lopez-Lozano, R., Jay, S., Marandel, R., Roy, M., Weiss, M., Li, W., Burger, P., Baret, F., 2019. A physically-based model to exploit UAV radiometric observations under heterogeneous illumination conditions. Presented at the 6th International Plant Phenotyping Symposium, Nanjing, China.

Lunagaria, M.M., Patel, H.R., 2019. Evaluation of PROSAIL inversion for retrieval of chlorophyll, leaf dry matter, leaf angle, and leaf area index of wheat using spectrodirectional measurements. International Journal of Remote Sensing 40, 8125–8145. https://doi.org/10.1080/01431161.2018.1524608

Ma Lu, S., Zainali, S., Stridh, B., Avelin, A., Amaducci, S., Colauzzi, M., Campana, P.E., 2022. Photosynthetically active radiation decomposition models for agrivoltaic systems applications. Solar Energy 244, 536–549. https://doi.org/10.1016/j.solener.2022.05.046

Madec, S., Irfan, K., Velumani, K., Baret, F., David, E., Daubige, G., Guo, W., De Solan, B., Chapman, S., Weiss, M., 2023. VegAnn: Vegetation Annotation of a large multi-crop RGB Dataset acquired under diverse conditions for image segmentation. Scientific Data in revision.

Magney, T.S., Eitel, J.U.H., Huggins, D.R., Vierling, L.A., 2016. Proximal NDVI derived phenology improves in-season predictions of wheat quantity and quality. Agricultural and Forest Meteorology 217, 46–60. https://doi.org/10.1016/j.agrformet.2015.11.009

Main, R., Cho, M.A., Mathieu, R., O'Kennedy, M.M., Ramoelo, A., Koch, S., 2011. An investigation into robust spectral indices for leaf chlorophyll estimation. ISPRS Journal of Photogrammetry and Remote Sensing 66, 751–761. https://doi.org/10.1016/j.isprsjprs.2011.08.001

May, R., Dandy, G., Maier, H., 2011. Review of Input Variable Selection Methods for Artificial Neural Networks, in: Suzuki, K. (Ed.), Artificial Neural Networks - Methodological Advances and Biomedical Applications. InTech. https://doi.org/10.5772/16004

Michalsky, J.J., Kiedron, P.W., 2022. Moderate spectral resolution solar irradiance measurements, aerosol optical depth, and solar transmission, from 360 to 1070 nm, using the refurbished rotating shadow band spectroradiometer (RSS). Atmos. Meas. Tech. 15, 353–364. https://doi.org/10.5194/amt-15-353-2022

Minolta, 2009. SPAD 502 MANUAL. Industrial Meter, Ramsey: Minolta Corp.

Niu, X., Fan, J., Luo, R., Fu, W., Yuan, H., Du, M., 2021. Continuous estimation of leaf area index and the woody-to-total area ratio of two deciduous shrub canopies using fisheye webcams in a semiarid loessial region of China. Ecological Indicators 125, 107549. https://doi.org/10.1016/j.ecolind.2021.107549

Ojha, T., Misra, S., Raghuwanshi, N.S., 2015. Wireless sensor networks for agriculture: The state-of-the-art in practice and future challenges. Computers and Electronics in Agriculture 118, 66–84. https://doi.org/10.1016/j.compag.2015.08.011

Oliphant, A.J., Stoy, P.C., 2018. An Evaluation of Semiempirical Models for Partitioning Photosynthetically Active Radiation Into Diffuse and Direct Beam Components. J. Geophys. Res. Biogeosci. 123, 889–901. https://doi.org/10.1002/2017JG004370

Peltoniemi, J.I., Kaasalainen, S., Näränen, J., Rautiainen, M., Stenberg, P., Smolander, H., Smolander, S., Voipio, P., 2005. BRDF measurement of understory vegetation in pine forests: dwarf shrubs, lichen, and moss. Remote Sensing of Environment 94, 343–354. https://doi.org/10.1016/j.rse.2004.10.009

Raj, M., Gupta, S., Chamola, V., Elhence, A., Garg, T., Atiquzzaman, M., Niyato, D., 2021. A survey on the role of Internet of Things for adopting and promoting Agriculture 4.0. Journal of Network and Computer Applications 187, 103107. https://doi.org/10.1016/j.jnca.2021.103107

Raymaekers, D., Garcia, A., Di Bella, C., Beget, M.E., Llavallol, C., Oricchio, P., Straschnoy, J., Weiss, M., Baret, F., 2014. SPOT-VEGETATION GEOV1 biophysical parameters in semi-arid agro-ecosystems. International Journal of Remote Sensing 35, 2534–2547. https://doi.org/10.1080/01431161.2014.883096

Rigon, J.P.G., Capuani, S., Fernandes, D.M., Guimarães, T.M., 2016. A novel method for the estimation of soybean chlorophyll content using a smartphone and image analysis. Photosynt. 54, 559–566. https://doi.org/10.1007/s11099-016-0214-x

Rogers, C., Chen, J.M., Croft, H., Gonsamo, A., Luo, X., Bartlett, P., Staebler, R.M., 2021. Daily leaf area index from photosynthetically active radiation for long term records of canopy structure and leaf phenology. Agricultural and Forest Meteorology 304–305, 108407. https://doi.org/10.1016/j.agrformet.2021.108407

Roosjen, P., Suomalainen, J., Bartholomeus, H., Kooistra, L., Clevers, J., 2017. Mapping Reflectance Anisotropy of a Potato Canopy Using Aerial Images Acquired with an Unmanned Aerial Vehicle. Remote Sensing 9, 417. https://doi.org/10.3390/rs9050417

Roosjen, P.P.J., Brede, B., Suomalainen, J.M., Bartholomeus, H.M., Kooistra, L., Clevers, J.G.P.W., 2018. Improved estimation of leaf area index and leaf chlorophyll content of a potato crop using multi-angle spectral data – potential of unmanned aerial vehicle imagery. International Journal of Applied Earth Observation and Geoinformation 66, 14–26. https://doi.org/10.1016/j.jag.2017.10.012

Roujean, J.-L., Lacaze, R., 2002. Global mapping of vegetation parameters from POLDER multiangular measurements for studies of surface-atmosphere interactions: A pragmatic method and its validation. J. Geophys. Res. 107, 4150. https://doi.org/10.1029/2001JD000751

Roujean, J.-L., Leroy, M., Deschamps, P.-Y., 1992. A bidirectional reflectance model of the Earth's surface for the correction of remote sensing data. J. Geophys. Res. 97, 20455. https://doi.org/10.1029/92JD01411

Ryu, Y., Verfaillie, J., Macfarlane, C., Kobayashi, H., Sonnentag, O., Vargas, R., Ma, S., Baldocchi, D.D., 2012. Continuous observation of tree leaf area index at ecosystem scale using upward-

pointing digital cameras. Remote Sensing of Environment 126, 116–125. https://doi.org/10.1016/j.rse.2012.08.027

Sánchez-Sastre, L.F., Alte da Veiga, N.M.S., Ruiz-Potosme, N.M., Carrión-Prieto, P., Marcos-Robles, J.L., Navas-Gracia, L.M., Martín-Ramos, P., 2020. Assessment of RGB Vegetation Indices to Estimate Chlorophyll Content in Sugar Beet Leaves in the Final Cultivation Stage. AgriEngineering 2, 128–149. https://doi.org/10.3390/agriengineering2010009

Sandmeier, S.R., 2000. Acquisition of Bidirectional Reflectance Factor Data with Field Goniometers. Remote Sensing of Environment 73, 257–269. https://doi.org/10.1016/S0034-4257(00)00102-4

Santos Valle, S., Kienzle, J., 2020. Agriculture 4.0 – Agricultural robotics and automated equipment for sustainable crop production. Integrated Crop Management Vol. 24, Rome, FAO.

Schaepman-Strub, G., Schaepman, M.E., Painter, T.H., Dangel, S., Martonchik, J.V., 2006. Reflectance quantities in optical remote sensing—definitions and case studies. Remote Sensing of Environment 103, 27–42. https://doi.org/10.1016/j.rse.2006.03.002

Serouart, M., Madec, S., David, E., Velumani, K., Lopez Lozano, R., Weiss, M., Baret, F., 2022. SegVeg: Segmenting RGB Images into Green and Senescent Vegetation by Combining Deep and Shallow Methods. Plant Phenomics 2022, 1–17. https://doi.org/10.34133/2022/9803570

Spitters, C.J.T., Toussaint, H.A.J.M., Goudriaan, J., 1986. Separating the diffuse and direct component of global radiation and its implications for modeling canopy photosynthesis Part I. Components of incoming radiation. Agricultural and Forest Meteorology 38, 217–229. https://doi.org/10.1016/0168-1923(86)90060-2

Uddling, J., Gelang-Alfredsson, J., Piikki, K., Pleijel, H., 2007. Evaluating the relationship between leaf chlorophyll concentration and SPAD-502 chlorophyll meter readings. Photosynth Res 91, 37–46. https://doi.org/10.1007/s11120-006-9077-5

Velumani, K., Madec, S., de Solan, B., Lopez-Lozano, R., Gillet, J., Labrosse, J., Jezequel, S., Comar, A., Baret, F., 2020. An automatic method based on daily in situ images and deep learning to date wheat heading stage. Field Crops Research 252, 107793. https://doi.org/10.1016/j.fcr.2020.107793

Verger, A., Vigneau, N., Chéron, C., Gilliot, Jean-Marc, Comar, A., Baret, F., 2014. Green area index from an unmanned aerial system over wheat and rapeseed crops. Remote Sensing of Environment 152, 654–664.

Verhoef, W., 1985. Earth observation modeling based on layer scattering matrices. Remote Sensing of Environment 17, 165–178. https://doi.org/10.1016/0034-4257(85)90072-0

Verhoef, W., 1984. Light scattering by leaf layers with application to canopy reflectance modeling: The SAIL model. Remote Sensing of Environment 16, 125–141. https://doi.org/10.1016/0034-4257(84)90057-9

Vermote, E.F., Tanre, D., Deuze, J.L., Herman, M., Morcette, J.-J., 1997. Second Simulation of the Satellite Signal in the Solar Spectrum, 6S: an overview. IEEE Trans. Geosci. Remote Sensing 35, 675–686. https://doi.org/10.1109/36.581987

Verrelst, J., Camps-Valls, G., Muñoz-Marí, J., Rivera, J.P., Veroustraete, F., Clevers, J.G.P.W., Moreno, J., 2015. Optical remote sensing and the retrieval of terrestrial vegetation bio-geophysical properties – A review. ISPRS Journal of Photogrammetry and Remote Sensing 108, 273–290. https://doi.org/10.1016/j.isprsjprs.2015.05.005

Verrelst, J., Malenovský, Z., Van Der Tol, C., Camps-Valls, G., Gastellu-Etchegorry, J.-P., Lewis, P., North, P., Moreno, J., 2019. Quantifying Vegetation Biophysical Variables from Imaging Spectroscopy Data: A Review on Retrieval Methods. Surv Geophys 40, 589–629. https://doi.org/10.1007/s10712-018-9478-y

Verrelst, J., Muñoz, J., Alonso, L., Delegido, J., Rivera, J.P., Camps-Valls, G., Moreno, J., 2012. Machine learning regression algorithms for biophysical parameter retrieval: Opportunities for Sentinel-2 and -3. Remote Sensing of Environment 118, 127–139. https://doi.org/10.1016/j.rse.2011.11.002

Verrelst, J., Rivera-Caicedo, J.P., Reyes-Muñoz, P., Morata, M., Amin, E., Tagliabue, G., Panigada, C., Hank, T., Berger, K., 2021. Mapping landscape canopy nitrogen content from space using PRISMA data. ISPRS Journal of Photogrammetry and Remote Sensing 178, 382–395. https://doi.org/10.1016/j.isprsjprs.2021.06.017

Wang, H., Wu, Y., Ni, Q., Liu, W., 2022. A Novel Wireless Leaf Area Index Sensor Based on a Combined U-Net Deep Learning Model. IEEE Sensors J. 22, 16573–16585. https://doi.org/10.1109/JSEN.2022.3188697

Wang, J., Lopez-Lozano, R., Weiss, M., Buis, S., Li, W., Liu, S., Baret, F., Zhang, J., 2022. Crop specific inversion of PROSAIL to retrieve green area index (GAI) from several decametric satellites using a Bayesian framework. Remote Sensing of Environment 278, 113085. https://doi.org/10.1016/j.rse.2022.113085

Wang, T., Gao, M., Cao, C., You, J., Zhang, X., Shen, L., 2022. Winter wheat chlorophyll content retrieval based on machine learning using in situ hyperspectral data. Computers and Electronics in Agriculture 193, 106728. https://doi.org/10.1016/j.compag.2022.106728

Weiss, M., Baret, F., 1999. Evaluation of Canopy Biophysical Variable Retrieval Performances from the Accumulation of Large Swath Satellite Data. Remote Sensing of Environment 70, 293–306. https://doi.org/10.1016/S0034-4257(99)00045-0

Weiss, Marie, Baret, F., Jay, S., 2020. S2ToolBox Level 2 products: LAI, FAPAR, FCOVER Version 2.1. INRAE, Avignon, France.

Weiss, M., Baret, F., Leroy, M., Hautecœur, O., Bacour, C., Prévot, L., Bruguier, N., 2002. Validation of neural net techniques to estimate canopy biophysical variables from remote sensing data. Agronomie 22, 547–553. https://doi.org/10.1051/agro:2002036

Weiss, M., Baret, F., Myneni, R.B., Pragnère, A., Knyazikhin, Y., 2000. Investigation of a model inversion technique to estimate canopy biophysical variables from spectral and directional reflectance data. Agronomie 20, 3–22. https://doi.org/10.1051/agro:2000105

Weiss, M., Baret, F., Smith, G.J., Jonckheere, I., Coppin, P., 2004. Review of methods for in situ leaf area index (LAI) determination. Agricultural and Forest Meteorology 121, 37–53. https://doi.org/10.1016/j.agrformet.2003.08.001

Weiss, M., Jacob, F., Duveiller, G., 2020. Remote sensing for agricultural applications: A meta-review. Remote Sensing of Environment 236, 111402. https://doi.org/10.1016/j.rse.2019.111402

Wu, B., Huang, W., Ye, H., Luo, P., Ren, Y., Kong, W., 2021. Using Multi-Angular Hyperspectral Data to Estimate the Vertical Distribution of Leaf Chlorophyll Content in Wheat. Remote Sensing 13, 1501. https://doi.org/10.3390/rs13081501

Xu, M., Liu, R., Chen, J.M., Liu, Y., Shang, R., Ju, W., Wu, C., Huang, W., 2019. Retrieving leaf chlorophyll content using a matrix-based vegetation index combination approach. Remote Sensing of Environment 224, 60–73. https://doi.org/10.1016/j.rse.2019.01.039

Yan, G., Hu, R., Luo, J., Weiss, M., Jiang, H., Mu, X., Xie, D., Zhang, W., 2019. Review of indirect optical measurements of leaf area index: Recent advances, challenges, and perspectives. Agricultural and Forest Meteorology 265, 390–411. https://doi.org/10.1016/j.agrformet.2018.11.033

Yang, D., Gueymard, C.A., 2020. Ensemble model output statistics for the separation of direct and diffuse components from 1-min global irradiance. Solar Energy 208, 591–603. https://doi.org/10.1016/j.solener.2020.05.082

Yang, X., Shi, H., Stovall, A., Guan, K., Miao, G., Zhang, Yongguang, Zhang, Yao, Xiao, X., Ryu, Y., Lee, J.-E., 2018. FluoSpec 2—An Automated Field Spectroscopy System to Monitor Canopy Solar-Induced Fluorescence. Sensors 18, 2063. https://doi.org/10.3390/s18072063

Yin, G., Li, A., Jin, H., Zhao, W., Bian, J., Qu, Y., Zeng, Y., Xu, B., 2017. Derivation of temporally continuous LAI reference maps through combining the LAINet observation system with CACAO. Agricultural and Forest Meteorology 233, 209–221. https://doi.org/10.1016/j.agrformet.2016.11.267

Zhang, P., Guo, Z., Ullah, S., Melagraki, G., Afantitis, A., Lynch, I., 2021. Nanotechnology and artificial intelligence to enable sustainable and precision agriculture. Nat. Plants 7, 864–876. https://doi.org/10.1038/s41477-021-00946-6

Zhang, R., Yang, P., Liu, S., Wang, C., Liu, J., 2022. Evaluation of the Methods for Estimating Leaf Chlorophyll Content with SPAD Chlorophyll Meters. Remote Sensing 14, 5144. https://doi.org/10.3390/rs14205144

Zhang, X., Jiao, Z., Zhao, C., Yin, S., Cui, L., Dong, Y., Zhang, H., Guo, J., Xie, R., Li, S., Zhu, Z., Tong, Y., 2021. Retrieval of Leaf Area Index by Linking the PROSAIL and Ross-Li BRDF

Models Using MODIS BRDF Data. Remote Sensing 13, 4911. https://doi.org/10.3390/rs13234911

Zheng, H., Cheng, T., Li, D., Zhou, X., Yao, X., Tian, Y., Cao, W., Zhu, Y., 2018. Evaluation of RGB, Color-Infrared and Multispectral Images Acquired from Unmanned Aerial Systems for the Estimation of Nitrogen Accumulation in Rice. Remote Sensing 10, 824. https://doi.org/10.3390/rs10060824

Zhou, X., Zhang, J., Chen, D., Huang, Y., Kong, W., Yuan, L., Ye, H., Huang, W., 2020. Assessment of Leaf Chlorophyll Content Models for Winter Wheat Using Landsat-8 Multispectral Remote Sensing Data. Remote Sensing 12, 2574. https://doi.org/10.3390/rs12162574